POLYMER/GLASS HOLLOW-CORE PHOTONIC BAND GAP FIBERS FOR INFRARED LASER BEAM DELIVERY

A THESIS
SUBMITTED TO THE GRADUATE PROGRAM OF MATERIALS
SCIENCE AND NANOTECHNOLOGY
AND GRADUATE SCHOOL OF ENGINEERING AND SCIENCE
OF BILKENT UNIVERSITY
IN PARTIAL FULFILLMENT OF THE REQUIREMENTS
FOR THE DEGREE OF
MASTER OF SCIENCE

By
Özlem Köylü
July, 2011

I certify that I have read this thesis and that in my opinion it is fully adequate, in scope and in quality, as a thesis for the degree of Master of Science.

Assist. Prof. Dr. Mehmet Bayındır (Advisor)

I certify that I have read this thesis and that in my opinion it is fully adequate, in scope and in quality, as a thesis for the degree of Master of Science.

Asst. Prof. Dr. Ali Kemal Okyay

I certify that I have read this thesis and that in my opinion it is fully adequate, in scope and in quality, as a thesis for the degree of Master of Science.

Asst. Prof. Dr. Selçuk Aktürk

Approved for the Graduate School of Engineering and Science:

Prof. Dr. Levent Onural
Director of the Graduate School

ABSTRACT

POLYMER/GLASS HOLLOW-CORE PHOTONIC BAND GAP FIBERS FOR INFRARED LASER BEAM DELIVERY

Özlem Köylü
M.S. in Materials Science and Nanotechnology
Supervisor: Assist. Prof. Dr. Mehmet Bayındır
July, 2011

Photonic band gap fibers are proposed for the medical applications of laser light transmission into body. Conventional optical fibers guide light via total internal reflection. Due to light guiding mechanisms and materials they have limited frequency range, fiber flexibility and laser power. On the other hand, it is possible to scale operating wavelengths of PBG fibers just by changing a few parameters during fabrication process. Besides, hollow core of PBG fibers eliminates material absorptions and non-linearities during light guiding.

PBG fiber production starts from material characterization; and selection; and continues with fiber design, thin film coating, preform preparation and fiber drawing. Studies on theoretical calculations and material properties have shown that best candidate materials for CO_2 laser delivery are As_2Se_3 and poly-ether-sulfone (PES). For this purpose, As_2Se_3 coated PES films are rolled to form a preform and consolidated before thermal drawing. Characterization of drawn fibers indicated that CO_2 laser can be transmitted with loss levels of > 1 dB/m and 32 W output power is observed from a 1.2 m long fiber.

After fabrication and characterization of PBG fibers, a prototype infrared laser system is built and tested on various applications. In our group laser tissue interactions are examined to see effectiveness of CO_2 laser on tumor tissue. Experiments showed that tumor tissue is affected in a very distinctive way compared to healthy tissue. Absorption of cancerous lung tissue at CO_2 laser wavelength (10.6 μm) is higher than absorption of healthy tissue at the same wavelength.

This study proposes a wide use of PBG fiber for not just CO_2 lasers, but also other laser systems used in different medical operations, such as Ho:YAG lasers. PBG fibers for high power laser delivery are novel structures for fast, painless and bloodless surgeries.

Keywords: Photonic Band Gap Fiber, Hollow-core Waveguide, Chalcogenide Glasses, Medical Lasers, High-Power Laser Beam Delivery.

ÖZET

FOTONİK BANT YAPILI KIZILÖTESİ LAZER İLETİMİ SAĞLAYAN POLİMER/KALKOJEN CAM İÇİ BOŞ FİBERLER

Özlem Köylü
Malzeme Bilimi ve Nanoteknoloji, Yüksek Lisans
Tez Yöneticisi: Yrd. Doç. Dr. Mehmet Bayındır
Temmuz, 2011

Bu çalışmada lazer ışını kullanılarak yapılan cerrahi müdahaleler için fotonik yasak banda sahip polimerik (PBG) fiberler önerilmiştir. Günümüzde kullanılan konvansiyonel fiberler, lazer ışınını basit indis farkı ile iletmekte ve bu dalga kılavuz yapısı ve malzeme özellikleri sebebiyle lazer operasyonlarında bazı kısıtlamalar getirmektedir. Bu kısıtlamalar lazer ışınının dalga boyunda, fiber esnekliğinde ve lazer gücünde gözlemlenmektedir. Diğer yandan fotonik bant yapılı fiberin iletim dalga boylarını sadece bir kaç üretim parametresini değiştirerek ayarlamak mümkün olmaktadır. Ayrıca, PBG fiberler içi boş olması sebebiyle malzeme kaynaklı ve doğrusal olmayan optik özelliklerden kaynaklanan güç kayıplarını önlemektedir.

PBG fiber üretimi malzeme karakterizasyonu ve seçimiyle başlar, fiber tasarımı, ince film kaplama, preform hazırlanması ve fiber çekimi ile devam etmektedir. Teorik çalışmalar ve malzeme özellikleri göz önüne alındığında CO_2 lazer iletimi yapan PBG fiber üretimi için en uygun malzeme çiftinin As_2Se_3 ve PES olduğu gözlemlenmiştir. Bu amaçla, As_2Se_3 kaplı PES filmi rulo oluşturacak şekilde sarılmış ve ısıl işlem uygulanarak bütünleştirilmiştir. Termal yolla çekilen fiberlerin karakterizasyonu gösterdi ki, bu yolla üretilen fiberler ile 1 dB/m'nin altında kayıpla lazer ışını iletilebilmektedir. Ayrıca, 1.2 m uzunluğundaki bir fiberden 32 W gücünde lazer iletimi de gözlemlenmiştir.

Fiber üretimi ve karakterizasyonundan sonra lazer-doku etkileşimleri incelenmiş ve CO_2 lazer ışınının tümörlü dokular üzerinde ayırıcı bir etkiye sahip olduğu görülmüştür. Grubumuzda yapılan ölçümler tümörlü akciğer dokusunun CO_2 lazer dalgaboyundaki soğurmasının sağlıklı dokuya göre daha yüksek olduğunu göstermiştir.

Bu çalışma gösterdi ki PBG fiberler sadece CO_2 lazerlerin değil, tıpta kullanılan diğer lazerler (Ho:YAG lazer gibi) içinde geniş bir kullanım alanı vaad etmektedir. Yüksek güçlü lazer ışınının iletimi için üretilen PBG fiberler acısız, kanamasız ve çabuk iyileşme süresine sahip cerrahi müdahaleller için sunulan ümit vaad eden yapılardır.

Anahtar sözcükler: Fotonik Bant Yapılı Fiberler, İçi Oyuk Dalga Kılavuzu, Kalkojenler, Medikal Lazerler, Yüksek güçlü lazer ışınının iletilmesi.

Acknowledgement

I am heartily thankful to my supervisor, Assist. Prof. Dr. Mehmet Bayındır, whose diligence, encouragement and especially patience from the beginning of my studies to my thesis defense. His experiences and guidance enabled me to develop an understanding of the subject.

I would like to thank my former group members; Dr. Mecit Yaman, Dr. Hakan Deniz and Dr. Abdullah Tülek for their insightful talks and role models as good scientists; Mert Vural for initiating this study; Ekin Özge Özgür for sample preparations, SEM images and investigation of laser-tissue interactions. I am also thankful to Mehmet Kanık for thin film coating and his help on fiber drawings; Tural Khudiyev for his help on simulations and use of supercomputers.

Additionally, I would like to thank my group members: Erol Özgür, Adem Yıldırım, Ozan Aktaş, and Reha Özalp for their instructive talks. I am also thankful to Neslihan Arslanbaba and Hülya Budunoğlu for being my closest friends and supporters especially during my MS studies. I also want to mention my former group members Duygu Akbulut, Özlem Şenlik, H. Esat Kondakçı, Kemal Gürel, Murat Kılınç, Yavuz N. Ertaş, Can Koral, Tarık Çeber and Ahmet Ünal. Engineers of National Nanotechnology Research Center Koray Mızrak, Mustafa Güler and Enver Kahveci were also very helpful during my studies.

Besides my present and former group members, I wish to give my special thanks to Prof. Dr. Salim Çıracı for being an elite scientist and for his efforts on founding National Nanotechnology Research Center together with my supervisor Assist. Prof. Dr. Mehmet Bayındır. I was a close witness of their struggle.

Finally, I am thankful to my husband Fahri Alkan, who is the greatest supporter and most important part of my life. Without him, I could not have complete this work. I am grateful for my family for their moral support.

I acknowledge The Scientific and Technological Research Council of Turkey, TUBITAK-BIDEB for the financial support during my graduate studies.

Contents

List of Figures

List of Tables

Chapter 1

Introduction

The idea of guiding light in air by using all-dielectric mirror is a promising area for high power laser delivery applications for about ten years [1, 2, 3]. Main idea here is to fabricate an hollow-core fiber with a dielectric mirror on the inner surface. The dielectric mirror here is basically a one dimensional photonic band gap structure. These air core and dielectric mirrors are novel structures of high power laser delivery fibers. In this work we present materials characterization, fiber design, fabrication principles, optical characterization, and use of hollow-core 1D PBG fibers for high power beam delivery for medical applications.

Hollow-core fibers basically consist of a dielectric mirror, which is alternating layers of two high refractive index-contrast materials, on its inner surface and a protecting cladding. Light guiding is provided with existence of radial bang gap in the dielectric mirrors and air core eliminates drastic losses from material absorptions and non-linearity effects arise from material properties and guiding structure [4]. Dielectric mirrors are fabricated with two different materials and there are two essential criteria for the material choice; the difference between the refractive indices should be high and thermomechanical properties of the materials should be similar.

The motivation of this thesis comes from that the fact that quarter wave stack (QWS) structures enable fabrication of omnidirectional mirrors [5]. Occurrence of optical band gap for a spectral range and for all incidence angles brings the idea of flexible 1D PBG fibers which can continue to function upon bending. In addition, air core is an advantageous property that current conventional solid-core optical fibers does not have. Light is guided by the dielectric mirror and air core constitutes low density medium which is more suitable for the high energy beam delivery. In addition to the high-power applications, the air core also provides gas phase sensing applications. For instance by using a binary system, sensing and differentiating different material vapors are possible [6]. Off-axis laser emission was also reported using cavity structures in radial direction [7].

CO_2 laser is first used in medical applications in late 1960s and today it is a very common technique for many surgery operations. Use of CO_2 laser is generally in the treatment of many cancer types. In these operations main purpose is to remove cancerous tissue by photothermal effect of CO_2 laser beam and reduce damage to neighboring tissues and organs [8].

Principle reason why CO_2 laser is very common in medicine world arises from laser-tissue interactions. Biological tissues include high amounts of water and water is highly absorptive at CO_2 laser wavelength 10.6 μm which is the frequency of vibrational modes of water molecules. Absorption of laser light by water molecules results in heat increase in the tissue, ablation and vaporization of tissue water [9]. Advantages of CO_2 laser compared to other commercial lasers used in medical applications are lower peak power, very small penetration depths and high optical absorption at 10.6 μm. Due to these properties, regions close to ablation site in the tissue are not affected by high laser power; and so, healthy tissue is preserved during the operation. Additionally, coagulation effects of CO_2 laser reduce blood loss and prevents edema formations after operation [10, 11]. Hence, patients can experience a painless and bloodless treatment and healing of the organ can take very short time.

The challenge of CO_2 laser use comes from laser beam guiding. Present commercial fibers for medical applications generally function in ultraviolet (UV), visible and near infrared (NIR) region of the optical spectra. New ways of light guiding for longer wavelength should be proposed since water absorption and laser-tissue interaction occur at longer wavelengths [10]. 1D photonic band gap (PBG) fibers are promising novel fibers for high power beam delivery to the operation site in the body [12]. However, fibers produced for such laser beams should be well designed and optimized for ultimate purpose of medical operation. For example, CO_2 laser delivery fibers should have a transmission band at 10.6 μm whereas Ho:YAG laser should have at 2.1 μm. CO_2 laser delivery PBG fibers are main focus of this study, therefore their design, fabrication, characterization and *in vitro* applications will be presented in this thesis staring from simple theory of light propagation.

Reports on the previous studies also shaped the progress of this study [12, 13, 14, 15]. In Chapter 2, the motivation of this work will be described in detail and the theoretical background in electromagnetics will be explained. Basic properties of dielectric mirrors, their band structures and one dimensional PBG in radial direction will be discussed in detail. Chapter 3 will be basically about general procedure of PBG fiber production. First, we will investigate material characterization. In the light of theoretical calculations and material properties design of the fiber and prediction of fabrication parameters will be explained. Production of PBG fibers will be explained step by step from the large area thin film coating to the thermal drawing. In Chapter 4, optical characterization of these fibers and the basic loss mechanisms will be examined. Also, CO_2 laser effects on various tissues will be reported in Chapter 5.

Chapter 2

Theoretical Background of Photonic Band Gap Fibers

2.1 Omnidirectional Reflection

Multilayered dielectric mirrors are basically one dimensional photonic crystals that can possess very high reflection of electromagnetic radiation. They are basically made up of two alternating dielectric materials with different refractive indices. Developments in deposition techniques yielded precise control of film layer thickness and also the control of the optical band gap of dielectric mirrors. These improvements led integration of dielectric mirrors to a variety of optical systems. Metallic mirrors are also used for similar applications. Although they have a very large spectrum range and omnidirectional reflection, they have some absorptions at high energetic part of the spectrum [16]. On the other hand, dielectric quarter wave stack (QWS) structures have metallic-like omnidirectional reflectivity and low-loss behavior. Additionally, they provide frequency selectivity by changing a few parameters during production process [5].

The idea of multilayered mirror is a known phenomena since 19^{th} century with the outstanding observations and calculations by Lord Rayleigh [17]. In

1917, Lord Rayleigh explained that the total reflection from a multilayered structure is the sum of all reflections from each interface [18]. Among many studies, the 1977 paper of Yeh *et. al.* is a crucial step for the explanation of the dielectric mirrors. In this paper, Yeh *et. al.* gives a general theory of reflection from a stratified media, which bases our calculations [19, 20]. However, omnidirectional reflection phenomena is first mentioned by Joannopoulos *et. al.* in 1998. Joannopoulos and his colleagues derived that if optical paths for two repeating materials in the multilayered mirror can be set to the half of wavelength, an angle- and polarization-independent optical band gap can be achieved [21, 22]. This improvement opens a gate for the fabrication of highly effective cavities and waveguides.

Light guiding in the hollow core fibers is achieved by multilayered dielectric mirrors. The mirrors inside the fibers are basically one dimensional structures in the radial direction. As stated before, for a 1D photonic crystal to have a omnidirectional band gap it is needed to use quarter wave stack (QWS) structures, by which optical paths in the alternating layers are both equal to half of the operating wavelength [5]. Eq. 2.1 gives the necessary layer thickness for a material; here, **n** is the refractive index and λ is the center wavelength of the optical band gap.

$$\mathbf{d} = \frac{\lambda}{\mathbf{4n}} \tag{2.1}$$

A dielectric mirror can be considered as a periodic array of dielectric interfaces. When one looks at the reflections from each interface the result can be very weak but the overall reflection from the structure can yield a large fraction of reflection. This overall reflection can be calculated by using a matrix formulation.

Basic structure can be illustrated as in Fig. 2.1 with the periodicity direction along the x axis. The refractive index of the structure as a function of x can be written as;

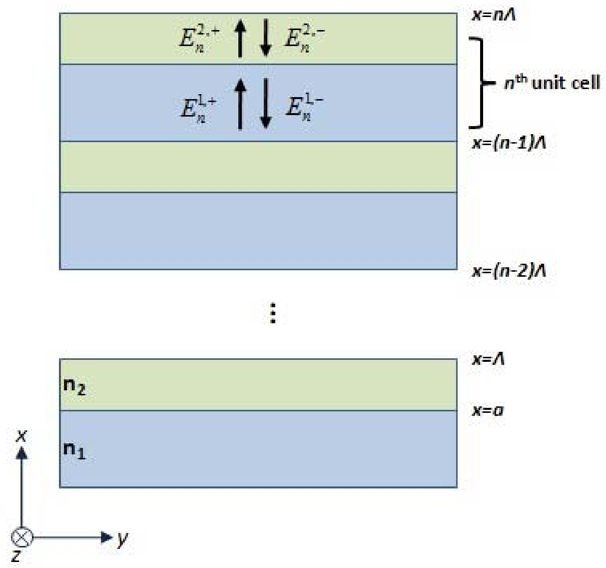

Figure 2.1: Schematic representation of a dielectric periodic medium and plane-wave amplitudes associated with n^{th} unit cell.

$$n(x) = \begin{cases} n_1, & \text{if } 0 < x < a \\ n_2, & \text{if } a < x < \Lambda \end{cases} \tag{2.2}$$

Here Λ is the period and $\Lambda = a + b$. The index function is a periodic function; i.e.

$$n(x) = n(x + \Lambda) \tag{2.3}$$

Then, electric field is written as;

$$E = E(x)e^{i(\omega t - k_z z)} \tag{2.4}$$

The x component of electric field for each layer is basically the sum of incident and reflected waves. Using this idea the x component of electric field for n^{th} pair can be defined as;

$$E(x) = \begin{cases} E_n^{1,+} e^{-ik_{1x}(x-n\Lambda)} + E_n^{1,-} e^{ik_{1x}(x-n\Lambda)}, & \text{if } n\Lambda - a < x < n\Lambda \\ E_n^{2,+} e^{-ik_{2x}(x-n\Lambda+a)} + E_n^{2,-} e^{ik_{2x}(x-n\Lambda+a)}, & \text{if } n\Lambda < x < (n-1)\Lambda - a \end{cases} \tag{2.5}$$

here;

$$\begin{aligned} k_{1x} &= k_1 \cos(\theta_1) = \tfrac{n_1\omega}{c} \cos(\theta_1), \\ k_{2x} &= k_2 \cos(\theta_2) = \tfrac{n_2\omega}{c} \cos(\theta_2). \end{aligned} \tag{2.6}$$

Here angles are the corresponding ray angles in the layers. Using matrix formulation we can write the relation between incident and reflected field coefficients in a column vector notation (Eq. 2.7 and Eq. 2.8).

$$\begin{pmatrix} E_{n-1}^{2,+} \\ E_{n-1}^{2,-} \end{pmatrix} = D_2^{-1} D_1 P_1 \begin{pmatrix} E_n^{1,+} \\ E_n^{1,-} \end{pmatrix} \tag{2.7}$$

and

$$\begin{pmatrix} E_n^{1,+} \\ E_n^{1,-} \end{pmatrix} = D_1^{-1} D_2 P_2 \begin{pmatrix} E_n^{2,+} \\ E_n^{2,-} \end{pmatrix} \tag{2.8}$$

where

$$P_j = \begin{pmatrix} e^{ik_{jx}d_j} & 0 \\ 0 & e^{-ik_{jx}d_j} \end{pmatrix}, \quad j = 1, 2 \ . \tag{2.9}$$

Dynamical matrices D_1 and D_2 are independent of layer thicknesses and P matrices give phase factors for each layer. After substituting these matrices and multiplication, we can obtain reflection relations for *s-polarized* waves as;

$$\begin{pmatrix} E_{n-1}^{1,+} \\ E_{n-1}^{1,-} \end{pmatrix} = \frac{1}{2} \begin{pmatrix} e^{ik_{2x}b}\left(1 + \frac{k_{2x}}{k_{1x}}\right) & e^{-ik_{2x}b}\left(1 - \frac{k_{2x}}{k_{1x}}\right) \\ e^{ik_{2x}b}\left(1 - \frac{k_{2x}}{k_{1x}}\right) & e^{-ik_{2x}b}\left(1 + \frac{k_{2x}}{k_{1x}}\right) \end{pmatrix} \begin{pmatrix} E_n^{2,+} \\ E_n^{2,-} \end{pmatrix} \tag{2.10}$$

and

$$\begin{pmatrix} E_n^{2,+} \\ E_n^{2,-} \end{pmatrix} = \frac{1}{2} \begin{pmatrix} e^{ik_{1x}a}\left(1+\frac{k_{1x}}{k_{2x}}\right) & e^{-ik_{1x}a}\left(1-\frac{k_{1x}}{k_{2x}}\right) \\ e^{ik_{1x}a}\left(1-\frac{k_{1x}}{k_{2x}}\right) & e^{-ik_{1x}a}\left(1+\frac{k_{1x}}{k_{2x}}\right) \end{pmatrix} \begin{pmatrix} E_n^{1,+} \\ E_n^{1,-} \end{pmatrix}. \tag{2.11}$$

Using Eq. 2.10 and Eq. 2.11, one can construct a matrix that relates amplitudes of the field at one pair to the next one;

$$\begin{pmatrix} E_{n-1}^{1,+} \\ E_{n-1}^{1,-} \end{pmatrix} = \begin{pmatrix} \breve{M}_{11} & \breve{M}_{12} \\ \breve{M}_{21} & \breve{M}_{22} \end{pmatrix} \begin{pmatrix} E_n^{1,+} \\ E_n^{1,-} \end{pmatrix}. \tag{2.12}$$

The matrix elements are;

$$\begin{aligned} \breve{M}_{11} &= e^{ik_{1x}a}\left[\cos k_{2x}b + \frac{1}{2}i\left(\frac{k_{2x}}{k_{1x}} + \frac{k_{1x}}{k_{2x}}\right)\sin k_{2x}b\right] \\ \breve{M}_{12} &= e^{-ik_{1x}a}\left[\frac{1}{2}i\left(\frac{k_{2x}}{k_{1x}} - \frac{k_{1x}}{k_{2x}}\right)\sin k_{2x}b\right] \\ \breve{M}_{21} &= e^{ik_{1x}a}\left[-\frac{1}{2}i\left(\frac{k_{2x}}{k_{1x}} - \frac{k_{1x}}{k_{2x}}\right)\sin k_{2x}b\right] \\ \breve{M}_{22} &= e^{-ik_{1x}a}\left[\cos k_{2x}b - \frac{1}{2}i\left(\frac{k_{2x}}{k_{1x}} + \frac{k_{1x}}{k_{2x}}\right)\sin k_{2x}b\right] \end{aligned} \tag{2.13}$$

Matrix $\breve{M}$ in Eq. 2.12 is the unit cell translation matrix which relates complex amplitudes of incident and reflected waves to the next unit cell. Using similar derivation one can find elements of translation matrix for TM waves as;

$$\begin{aligned} \breve{M}_{11}^{TM} &= e^{ik_{1x}a}\left[\cos k_{2x}b + \frac{1}{2}i\left(\frac{n_2^2k_{1x}}{n_1^2k_{2x}} + \frac{n_1^2k_{2x}}{n_2^2k_{1x}}\right)\sin k_{2x}b\right] \\ \breve{M}_{12}^{TM} &= e^{-ik_{1x}a}\left[\frac{1}{2}i\left(\frac{n_2^2k_{1x}}{n_1^2k_{2x}} - \frac{n_1^2k_{2x}}{n_2^2k_{1x}}\right)\sin k_{2x}b\right] \\ \breve{M}_{21}^{TM} &= e^{ik_{1x}a}\left[-\frac{1}{2}i\left(\frac{n_2^2k_{1x}}{n_1^2k_{2x}} - \frac{n_1^2k_{2x}}{n_2^2k_{1x}}\right)\sin k_{2x}b\right] \\ \breve{M}_{22}^{TM} &= e^{-ik_{1x}a}\left[\cos k_{2x}b - \frac{1}{2}i\left(\frac{n_2^2k_{1x}}{n_1^2k_{2x}} + \frac{n_1^2k_{2x}}{n_2^2k_{1x}}\right)\sin k_{2x}b\right] \end{aligned} \tag{2.14}$$

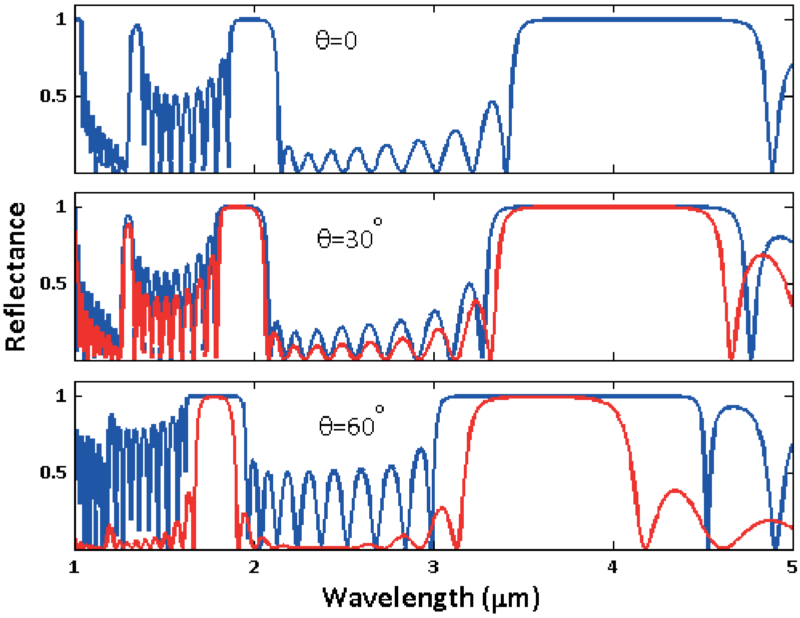

Figure 2.2: Spectral dependance of the reflectance R for the 10-segment dielectric mirror with n_1=1.5, n_2=2.5 and Λ=1 μm. Reflection profile for TE and TM polarisations does not differ for normal incidence. For 30° and 60° incidence angles they have different profile. Blue lines indicate TE polarisation and red lines indicate TM polarisation.

The translation matrix for the N-segment structure is multiplication of the translation matrix for all segments. Thus, one can write Eq. 2.15 which relates complex field amplitudes of the incident wave in the isotropic ambient medium to the end of the structure [20].

$$\begin{pmatrix} E_N^{1,+} \\ E_N^{1,-} \end{pmatrix} = \begin{pmatrix} M_{11} & M_{12} \\ M_{21} & M_{22} \end{pmatrix}^{-N} \begin{pmatrix} E_0^{1,+} \\ E_0^{1,-} \end{pmatrix}. \tag{2.15}$$

Eq. 2.15 opens a gateway to all optical properties of the combined system. The ratio between coefficients of the reflected and incident components of electric field will give us reflectivity of the system (Eq. 2.5) and the back propagating component of the field at the end of the mirror will be zero i.e. $E_N^{1,-} = 0$. Using this information and the components of the matrix M which is N^{th} power of the matrix $\check{M}$, one can find the reflection constant as in Eq. 2.16 and 2.17.

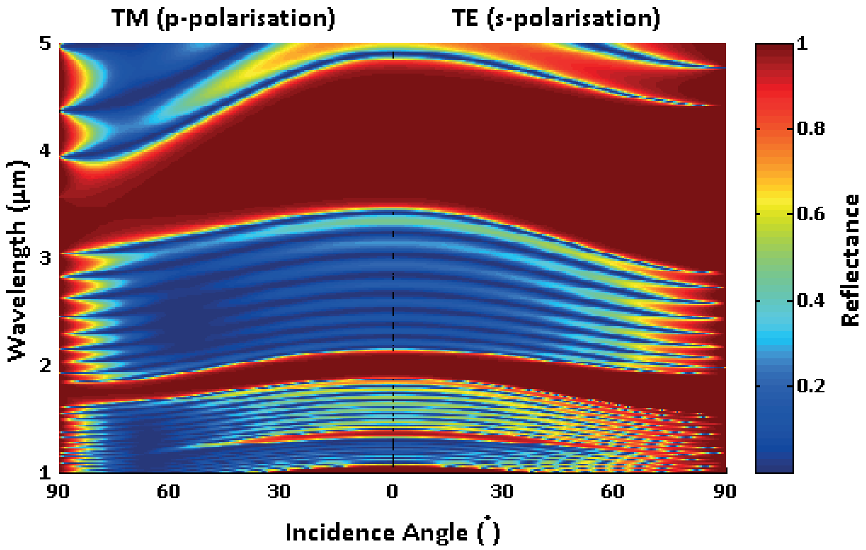

Figure 2.3: The reflectance profile of a layered dielectric structure for both polarizations and whole incidence angle range with n_1=1.5, n_2=2.5 and N=10.

$$r_N = \left(\frac{E_0^{1,-}}{E_0^{1,+}} \right) \tag{2.16}$$

and

$$r_N = \frac{M_{21}}{M_{11}}, \quad R = |r_N|^2 = \left| \frac{M_{21}}{M_{11}} \right|^2 \tag{2.17}$$

The last equation, together with Eq. 2.13 and 2.14 gives the relation between the frequency of the incident wave and the reflectance of the dielectric mirror [20]. Fig. 2.2 is a characteristic reflectance behavior for a sample mirror with N=10, n_1=1.5, n_2=2.5 and $a = b = \Lambda/2$. The sample structure has different reflection bands for different frequency, each of them corresponds to different orders of band gap. A noteworthy property is the gap for TE mode gets wider as the incidence angle increases whereas the width of the gap for TM mode gets smaller as it can be seen from Fig. 2.3. Therefore, one can conclude that the width of omnidirectional band gap is determined by the width of the gap of TE mode at normal incidence plus the width of the gap of TM mode at 90°. However, the sample structure here does not have an QWS structure and the optical gap for TM mode shifts from the normal incidence gap range.

2.2 Band Structures

Electrons' motion in a crystalline solid is very similar to wave propagation in periodic media [20, 23]. Therefore, using same methodology one can construct a similar band theory for wave motion in periodic dielectric media and some of the physical concepts such as Bloch waves, forbidden and allowed bands can be used. Basically, a periodic layered media is mathematically same as one dimensional lattice and *optical potential* i.e. the refractive index of the media is invariant under translation: $n(x+\Lambda) = n(x)$. This methodology gives periodic solutions to the wave equations and there is only a lattice translation factor between two consecutive pairs (Eq. 2.18).

$$\begin{pmatrix} E_n^{1,+} \\ E_n^{1,-} \end{pmatrix} = e^{-iK\Lambda} \begin{pmatrix} E_{n-1}^{1,+} \\ E_{n-1}^{1,-} \end{pmatrix} \tag{2.18}$$

From Eq. 2.12 and 2.18 problems become an eigenvalue problem [19]:

$$\begin{pmatrix} M_{11} & M_{12} \\ M_{21} & M_{22} \end{pmatrix} \begin{pmatrix} E_n^{1,+} \\ E_n^{1,-} \end{pmatrix} = e^{iK\Lambda} \begin{pmatrix} E_n^{1,+} \\ E_n^{1,-} \end{pmatrix} \tag{2.19}$$

Here K is Bloch wave number and the expression $e^{-iK\Lambda}$ corresponds to the phase shift of the electromagnetic wave propagating along the lattice. Eigenvalues of Eq. 2.19, which are solutions to the Bloch wave numbers determine the propagation behavior of electromagnetic wave i.e. the real solutions of K correspond to the waves that can propagate and complex solutions correspond forbidden waves. The solutions of the Bloch wave numbers are given in the following expression:

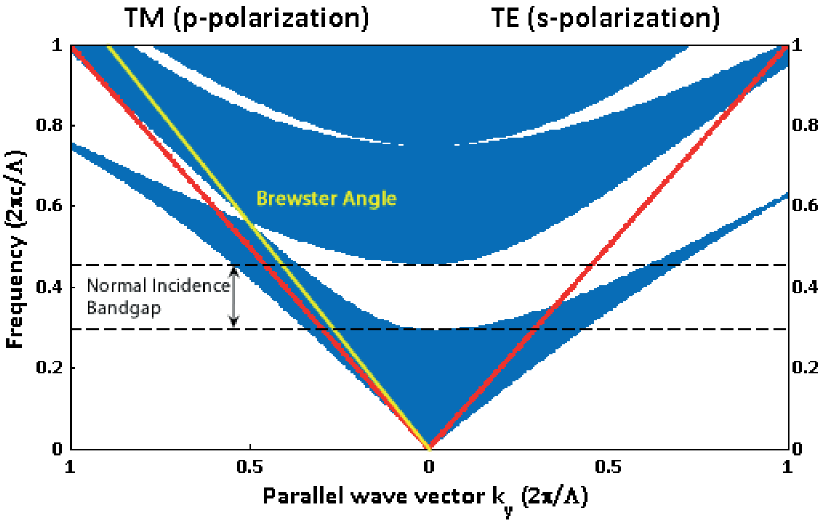

Figure 2.4: Band structure of a typical periodic layered medium in the normalized $\omega - k_y$ plane with n_1=2 and n_2=1 for both TE and TM polarizations. The blue regions are allowed bands with $|\cos K\Lambda| < 1$ while white regions represent the forbidden bands. The red line represents the *Light Line*.

$$\cos K\Lambda = \cos k_1 a \cos k_2 b - \frac{1}{2}\left(\frac{n_2}{n_1} + \frac{n_1}{n_2}\right) \sin k_1 a \sin k_2 b \tag{2.20}$$

where

$$K = \sqrt{k_x^2 + k_y^2}$$

and Fig. 2.4 represents the projected band diagram of a QWS structured periodic media (i.e. $d_1/d_2 = n_2/n_1$). In the figure, the red line represents the *Light Line* which is determined by $\omega = cK$. Originally we are interested in the waves that are originating from a homogenous medium which is air. Hence, only the region above the light line is important for our case, i.e. below the light line area are trivially forbidden bands. Here, k_y =0 corresponds to normal incidence and k_y values lying on the light line corresponds to 90° incidence. For this structure there is an optical band gap for normal incidence. An interesting result is that TM forbidden bands shrink to zero as incidence angle gets to a specific angle.

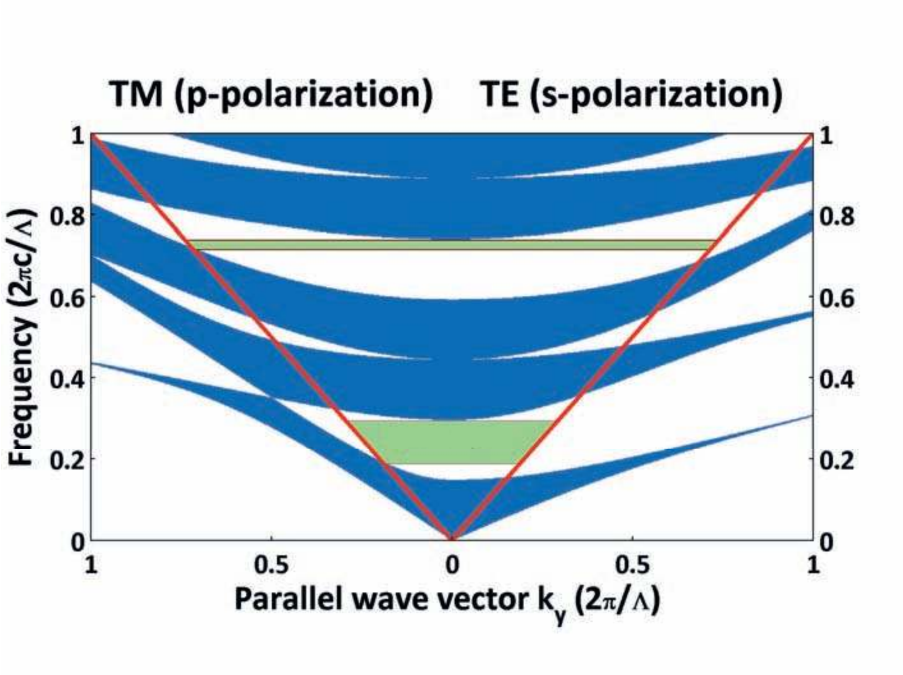

Figure 2.5: Band structure of an omnidirectional reflector with n_1=4.5 and n_2=1.5 for both TE and TM polarizations. The green regions represents first order and second order omnidirectional forbidden band.

This angle value is called Brewster Angle (yellow line in the figure). Fig. 2.5 is another example structure (n_1=4.5 and n_2=1.5) which has omnidirectional forbidden bands (green regions) for both polarizations. Here, an important feature is the difference between refractive indices which affects the width of the band region. Higher the refractive index contrast, wider the forbidden gap. Additionally, high refractive index contrast lead to shorter evanescent wave decay lengths and decrease material-light interaction; hence, decreased material losses.

As explained above, in order to have an omnidirectional reflection the ratio of layer thicknesses should be equal to the reciprocal of the ratio of indices. An important property is one can adjust central frequency of the band gap using Eq. 2.1. This feature provides an important way to design many dielectric structures for a variety of applications [12, 13, 14, 24]. In solid crystals impurities can cause scattering and absorptions. A similar phenomenon is also exists in dielectric mirrors. Impurities in the layer thicknesses of the structure can lead to filtering effects for particular frequencies [25, 26]. Such properties of layered dielectric structures provide a large area of applications from optical communication systems and display systems to medical applications.

2.3 Cylindrical Geometry

Today's communications systems are mainly depend on waveguides which transport light for very long distances with very small losses. Simple structure of an optical fiber is a core-cladding structure in which light is guided with total internal reflection (TIR) [27]. The most known example of this kind is conventional silica fibers which are known as *index guiding fibers*. Embedding different structures and different materials to the fibers enables the usage of fibers in a wide range of applications [23, 27, 28]. For instance, improving glass drawing methods led to solid and air core photonic crystal glass fibers [29, 30, 31, 32]. In addition to core-cladding and photonic crystals glass fibers, applying a one dimensional dielectric mirror as explained above results in a light guiding due to the photonic band gap in the radial direction [1]. Main materials used for the fabrication of photonic band gap fibers are basically chalcogenide glasses and polymers [12].

2.3.1 Index Guiding Waveguides

Simple index guiding fibers are the basis for most of the telecommunication lines. Main reason is the ease of fabrication of these fibers and low loss levels at optical frequencies. Propagation of light through these fibers is basically due to total internal reflection between core and cladding structures with indices n_1 and n_2. Mathematical solution simply comes from Snell's Law;

$$n_1 \sin\theta_1 = n_2 \sin\theta_2 \tag{2.21}$$

The critical angle for the structure can be found by setting the refraction angle to 90°. Thus the critical angle for the structure can be found as;

$$\theta_c = \sin^{-1}\left(\frac{n_2}{n_1}\right) \tag{2.22}$$

This means propagating light which has an incidence angle bigger than θ_c encounters a complete reflection. Hence, refractive indices of core and cladding materials determine the angle window of total reflection. From Eq. 2.22 one can conclude that to have a total internal reflection light guiding index of the core should be higher than the cladding. Accordingly, guiding light in air is very difficult and losses due to material absorptions and dispersion becomes significant. Another difficulty for these fibers are mechanical properties of materials. Generally core-cladding structure fibers are made of rigid materials and so, fibers have a limited flexibility. The most common material for TIR fibers is silica because of its low absorptions at 1.55 μm, which is the wavelength that most of the optical communications systems operate. Basically both core and cladding are isotropic media and light guiding occurs in the region where both of the materials' light cones intersect. A simple representation is in Fig. 2.6 for a typical silica fiber with core index 1.5 and cladding index 1.45.

The light waves coupled into the fiber has different propagation angles. Each of these propagation angles constitutes different *mode*s. Each waveguide depending on its geometry, dimensions and other optical properties allows single or multi modes. A single mode fiber has a very small core (on the order of the wavelength) that the light wave does not have enough room to bounce off. Hence, in a single mode fiber light wave travels straight in the core of the fiber.

2.3.2 Photonic Band Gap Fibers

Photonic band gap fibers basically guides light by band gaps in different directions in the structure. The reflection mechanism and the band structure of dielectric structures are explained in sections 2.1 and 2.2. For waveguide and fiber structures geometry is two or three dimensional. Different periodicity in multi dimensions or cavity structures covered with mirrors constitutes small conduits for the propagation of light.

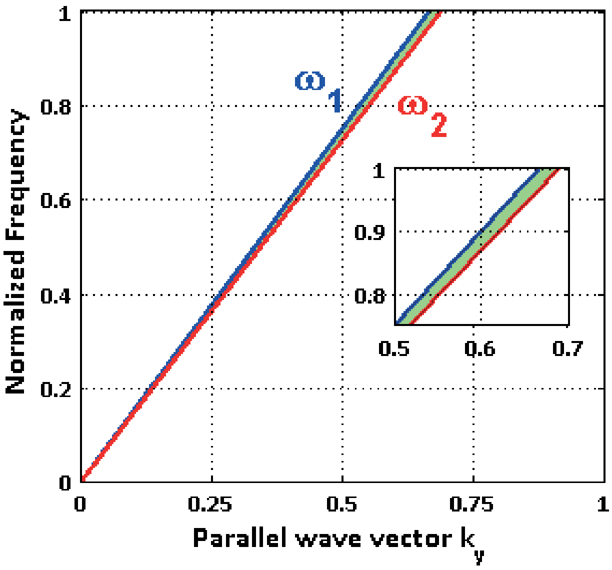

Figure 2.6: The propagation allowed light cones of the a conventional silica fiber with n_{core}=1.5 (ω_1) and n_{clad}=1.45 (ω_2). The green area between light lines is the propagation bands for the fiber structure.

As the optical signal transportation and integrated optical circuits continues to develop optical waveguide structures conserve its importance. Basic obstacles for the area is elasticity of the waveguide structures and loss mechanisms. As mentioned above, materials' properties and limited guidance angle is a big problem for optical silica fibers. A similar problem is seen at metallic fibers that bending fibers increase loss due to absorptions. Hence, both TIR and metallic fibers have a very large critical radius of curvature. These reasons lead to an increasing interest in dielectric photonic band gap waveguides and fibers.

Photonic band gap structures can be grouped due to their periodicities: one dimensional, two and three dimensional. From the analogy of the solid crystals one can think these photonic structures as *photonic crystals*. One dimensional photonic crystals are basically layered structures which are explained in the previous sections. Waveguide is constructed by trapping light in two dimensions, the structure is isotropic in two dimensions and the light guiding occurs in these directions (Fig. 2.7a) [33]. A two dimensional photonic crystal has periodicity in two dimensions and isotropic in the third dimension. Similarly, light guiding

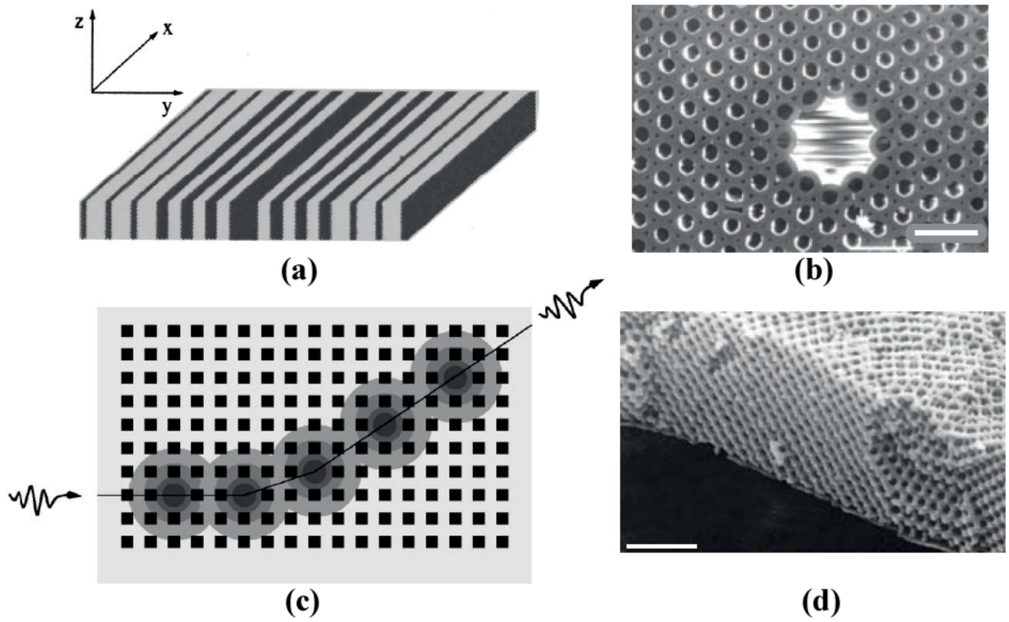

Figure 2.7: (a) Waveguide structure with one dimensional photonic crystal guiding. Light propagation is in the x-direction. (b) An electron microscopy image of a hollow-core photonic band gap fiber. (c) Schematic illustration of propagation of electromagnetic waves hopping between the coupled evanescent defect modes on a bended path. (d) SEM image of the 3D photonic crystal which creates a bright green colour on the scales of *Parides sesostris*. Scale bars; (b) 10 μm, (d) 1.2 μm. Adopted from; (a) Taniyama [33], (b) Knight [30], (c) Bayindir [34], (d) Vukusic [35]

can occur in the isotropic direction. Two dimensional photonic crystals fibers are prominent examples of this kind of waveguides (Fig. 2.7b). Another light guiding mechanism in the 2D photonic crystals is using defects. An example can be seen in Fig. 2.7c. Using a series of cavities in close vicinity makes it possible to construct a defined path for the propagation of light at certain frequencies [30, 34, 36]. These wave guiding mechanism is widely used in integrated optical circuits and it is possible to make the electromagnetic wave to pass through 90° corners. In 1991 Yablonovic and Gmitter fabricated first three dimensional photonic crystal with a complete band gap [37]. Functioning wavelength for the structure was at microwave but the following studies showed that it is possible to adjust the structure for particular wavelength by using different pitch size and different geometries [28]. There is an interesting example of three dimensional

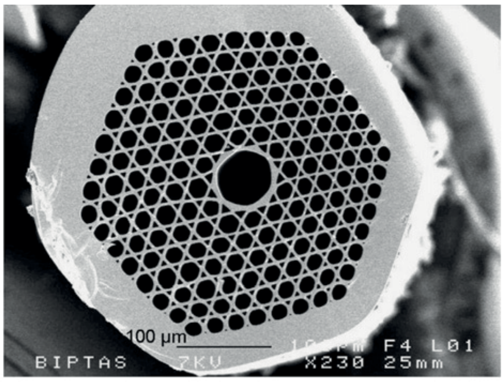

Figure 2.8: An SEM image of a chalcogenide 2D PCF with kagome lattice. Scale bar 100 μm. Adopted from, Desevedavy [40].

photonic band gap structures in nature, on the scales of certain butterflies. For instance, Fig. 2.7d is an SEM image of photonic structures on the scales of *Parides sesostris*. The structure is very close to tetrahedral structure which is resulting in a very bright green color [35]. However, wave guiding in 3D crystals is again due to the cavity structures in close vicinity in three dimensions [38, 39].

A fiber is basically a two dimensional structure which is generally examined in polar coordinates. Their properties along their length is considered as the same extending to infinity since their aspect ratio is very high. Hence, optical properties of these fibers are examined only for cross sections. Optical fibers can be also used for different applications apart from wave guiding; however, main application examined and used in this thesis is propagation of electromagnetic wave through the fiber. The simplest form of the optical fibers are the core-cladding structured fibers which are explained in the previous sections. Besides TIR fibers, there are fibers in which guiding is done by photonic band gap. These photonic band gap structures has periodicity in radial or both in radial and angular directions. In the last few decades development in fabrication methods gave the advantage of guiding electromagnetic waves in air-cores. Air guiding is advantageous compared to solid core fiber because of non-linearity effects. In air the losses due to non-linearities are mostly eliminated. For example, a recent study shows an example of chalcogenide glass 2D photonic crystal fibers with a few dB losses (Fig. 2.8) [40]. Common material for the 2D PCF is silica. However, these type of fibers are

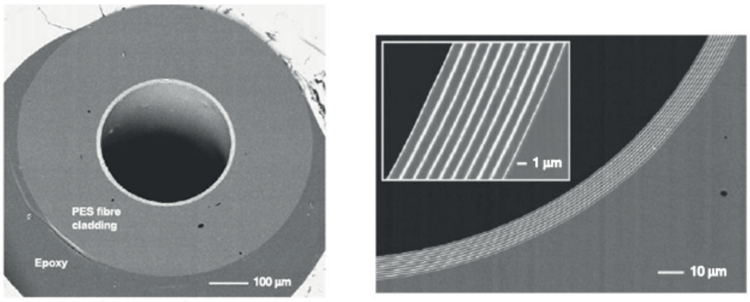

(a) (b)

Figure 2.9: SEM image of cross-section of a hollow-core 1D PCF with PES/As_2Se_3 alternating layers. The fundamental band gap is at 3.55 μm. Adopted from, Temelkuran [12].

generally used for high frequency waves . On the other hand chalcogenide glasses have promising optical properties in the infrared region but 2D chalcogenide gals fibers are very new area.

One dimensional photonic crystal fibers are the main subject of this thesis and they have a simpler structure compared to 2D PCFs. In 1D PBG fibers, periodicity is along the radial direction; and hence, there is a band gap in all polar directions. Basic structure of the fiber is periodic dielectric layers around the air core with high and low index materials. Low index material is polymer and high index material is chalcogenide glass which have similar thermo-mechanical properties around the drawing temperature (explained in detail in Chapter 3). Fig. 2.9 is an electron micrograph image with alternating layers of PES and As_2Se_3 with fundamental band gap at 3.55 μm. Ease of fabrication and working wavelength and hollow core makes these fibers promising candidates for high power laser beam delivery especially for medical applications [41, 10].

An important property of these structures is as long as QWS ratio is preserved between the layer thicknesses, it is possible to adjust the center frequency of the fundamental omnidirectional band gap. This property allows to fabricate different fibers, each working at different frequency, from one drawing process.

Chapter 3

Production of Photonic Band Gap Fibers

The extensive fabrication method of conventional optical fibers is thermal drawing [31, 42]. This method is also used for the fabrication of photonic band gap fibers (PBG) even for the ones with hollow-core [4, 43, 30]. Studies have shown that thermal drawing is a reliable fabrication method for multi-material PBG fibers as well [12, 13, 15, 44]. However, drawing is done at high temperatures where the materials are viscous. Hence, characterization of materials' properties becomes very important to ensure material compatibility for both fabrication and optical performance of the fiber. Besides, fabrication process should be revised for the composite fiber fabrication.

In Chapter 2 necessity for high-index contrast for the optimum photonic band is explained. For the fabrication purposes, thermomechanical properties of materials should be examined; material preference and fabrication parameter settings should be done accordingly. This chapter will focus on basic material properties necessary for successful fiber fabrication. We will first focus on the candidate materials and then we will look at their optical and thermo-mechanical properties. Then we will adapt the conventional method for the new materials and focus on production of PBG fibers.

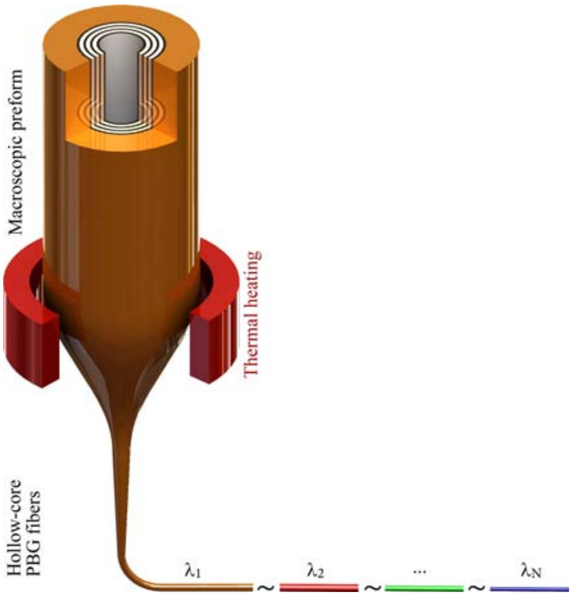

Figure 3.1: Thermal drawing is basically reducing feature size of a macro structure to micro scale at softening temperatures of materials. Figure is an image of schematics of 1D PBG fiber drawing.

The thermal drawing method used for conventional fiber fabrication has been a well established method for the last few decades. However, the method is generally used for glass and single material fibers. In the last decade studies are focused on fabrications of composite fibers for a variety of purposes and with very small feature size [12, 44, 15, 45]. The reason for big interest in thermal drawing arises from the fact that it is commonly used in industry and it allows to produce kilometer-long fibers with consistent properties in a very short time. Reports have shown that there are other methods to fabricate such composite small featured fibers [46, 47]; but, these methods are generally used for fabrication of very small laboratory scale samples [48]. Therefore, the focus of this chapter will be characterization of candidate materials and choice of the optimum set of materials which have compatible properties for both fabrication purposes and optical functions. Mostly our focus will be on enhancement of overall production process from the thin film production to the end product.

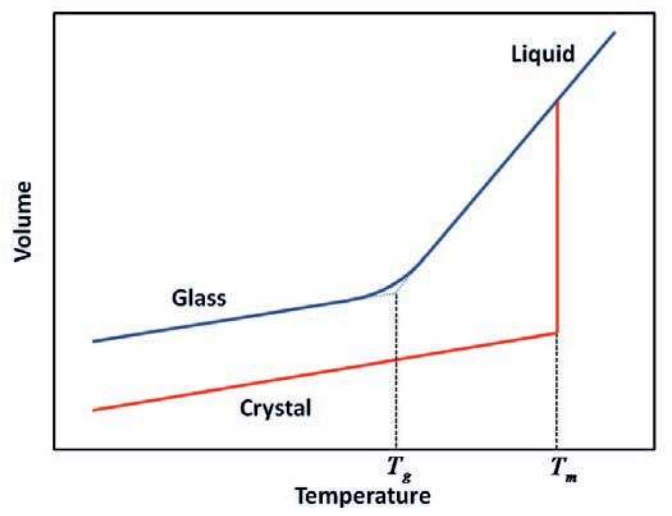

Figure 3.2: Schematic illustration of volume dependence temperature of a glass and a crystalline phases of a typical material. Here T_m is melting temperature and T_g is glass transition temperature.

3.1 Materials Characterization

Glass or glassy materials are typical materials for thermal drawing processes due to their amorphous structure. Basically, amorphous materials do not have long range symmetry and this feature allows them to experience a continuous phase change upon heating. Crystals on the other hand have sudden changes in their properties such as volume and viscosity during the phase change from solid to liquid. Hence, amorphous or glassy materials are the best candidates for controlled mechanical deformation at high temperatures [49]. Therefore, one should choose glassy materials which will remain amorphous during the thermal processes such as thermal deposition and drawing. Fig. 3.2 illustrates a typical volume change of an amorphous material and a crystalline material.

The quasi-continuous change in viscosity is an advantage for fabrication of composite materials since it enables use of inorganic glasses and organic polymers at the same time [49, 50, 51]. However, there are some constraints in the fabrication of glassy/thermoplastic composite structures. For instance, during thermal processes viscosities of materials must be close and they should experience similar plastic deformation under stress. In addition, adhesion of materials must be high during evaporation and remain same during drawing and end product.

The dielectric properties of the materials are another important aspect for efficiency of fibers. After the production processes complete, the end product should have a large optical band gap and low penetration depth to eliminate material absorption. As stated earlier, this can be achieved by having high refractive index contrast material sets. Although in some studies it is claimed that high index contrast is limited for material sets that have similar thermomechanical properties [52], the studies afterwards indicated that it is possible to have very different materials showing similar thermoplastic properties and having high index contrast [45]. Besides index contrast, low absorption property is also required from the materials. The objective of this study is transmitting high power CO_2 laser beam. Hence, materials of interest should have no or very low absorption levels on the infrared region, especially around 10.6 μm.

Considering all the criteria mentioned above, best material choice will be chalcogenide glasses. Chalcogenide glasses are amorphous structures that contain Group-16 elements such as; selenium, sulfur and tellurium [53]. These materials generally have high refractive indices. Depending on the composition there are a big variety of chalcogenide materials. Basically they are categorized depending on their elemental composition; eg. two-, three- or four-component systems [54]. An important property is that chalcogenide glasses generally do not contain oxygen which is an advantage to work in high temperatures. In this study the candidate chalcogenide glasses are commercially available As_2Se_3 and As_2S_3 which have infrared transparency (i.e. lossless in IR region). Another candidate is a four-component system contains Ge, As, Se and Te.

The composition of chalcogenide glasses affect important properties of these materials. For example, electronic structure of an element determines its coordination number and tendency of cross-linking. As the cross-linking increase the degrees of freedom of atoms decrease and results in raise of softening point of the material [45, 54]. For instance, it has been reported that $\mathrm{As_{40}Se_{60}}$ glass has a viscosity value of 10^{13} Pa×s at temperature 170 °C, albeit $\mathrm{As_{40}Ge_{10}Se_{50}}$ has at 211 °C and $\mathrm{As_{40}Ge_{35}Se_{25}}$ has at 406 °C [54]. Here Ge has 4 coordination number and hence, it has a dense bond network with the surrounding atoms resulting in an increase in melting point of the glass. Another effect is atomic weights of components. Adding heavier composites to the material results in an decrease in glass transition temperature. The atoms with bigger atomic numbers has lower binding energy for their outer shell. Hence, their valance electrons has higher tendency toward polarization. This relation emerges an increase in dielectric constant, whereupon the refractive index. For example, As_2Se_3 has a dielectric constant of 9.92 and when thallium including composite glass (20 at.%) has a dielectric constant of 22.3 [54]. In general chalcogenide glasses have high refractive indices and they are very good candidates for high index material for the multi-material fiber.

For the low index material one can have different material candidates such as other glassy materials. For instance, SiO_2 which is used for conventional optical fibers. However, even though it is possible to change the melting point with different impurities, still the softening point of such oxide glasses are very high compared to chalcogenide glasses (in the range 750 - 1700 °C). Another material class is thermoplastic polymers since they have amorphous structure and are easy to process. Nonetheless, majority of these polymers have very low softening points except some commercial thermoplastics such as poly(ether-sulfone)(PES) or poly(ether-imide)(PEI). Measurements have shown that these materials have similar softening points with some simple structured chalcogenide glasses such as As_2Se_3 and As_2S_3 (Fig. 3.3).

In this study material set examined and studied in detail is as follows; high index material: As_2Se_3, As_2S_3 and $Ge_{15}As_{25}Se_{15}Te_{45}$ (GAST), low index material: PES, PEI. The following section of this chapter is about thermomechanical and optical characterization of these materials. Basically, glass transition, viscosity, wettability of materials and optical constants are determined for the optimization of production process.

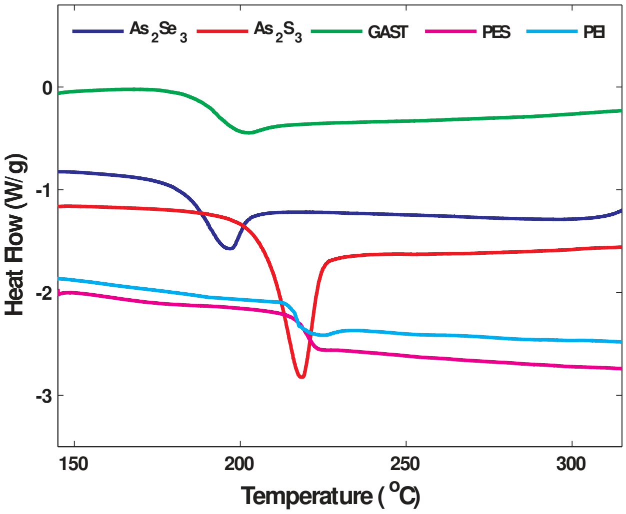

Figure 3.3: The DSC data of the materials set: chalcogenide glasses; As_2Se_3, As_2S_3 and GAST. polymers; PES and PEI

3.1.1 Thermomechanical Properties

Thermal fiber drawing process requires a series of heat treatments and the last step requires a thermo-mechanically compatible material set. Hence, thermal behavior of materials should be examined for production of PBG fibers. For instance, for safety of the fabrication structure of materials should remain amorphous. Additionally, glass transition and softening points of the materials should be measured. Fig. 3.3 is Differential Calorimetry System (DSC) data of our material set. Steps on the curves represent glass transition temperatures of materials which are; for $\mathrm{As_2Se_3}$ T_g=189 °C, for $\mathrm{As_2S_3}$ T_g=209 °C, for GAST T_g=193 °C, for PES T_g=220 °C, and for PEI T_g=217 °C. Hence, it is confirmed that all of these materials have similar glass transition temperatures. The values are close enough to work. Basically Fig. 3.3 is a measure that all these materials have similar softening points.

An important property for the process is the viscosities of the materials depending on the temperature. Viscosity is basically a resistance of materials to flow under applied stress. One of the first mathematical definitions of viscosity is made by Trouton in 1906. Trouton defined viscosity as the ratio of applied stress to the change in strain as given is Eq. 3.1 [55];

$$\eta \propto \sigma / \left(\frac{d\epsilon}{dt} \right) \tag{3.1}$$

When this proportionality is constant, i.e. viscosity is independent of stress and strain, such materials are called Newtonian fluids. In this study, however, all the materials are non-Newtonian and viscosities are generally depend on applied stress. Previous studies have shown that estimating the viscosities using models for Newtonian fluids are enough for the design of he fabrication process [45].

Due to the structural differences in glassy materials and thermoplastic polymers, models for estimation of viscosity values are differ for these materials. For instance a study in 2003 gives some simple relations for the viscosities of glassy chalcogenides [56]. Tverjanovich reported that viscosity of chalcogenide glasses has a general form:

$$\eta = \eta_0 \exp\left(E_n / RT\right) \tag{3.2}$$

Here, E_n is the activation energy and η_0 is exponential constant. Activation energy can be calculated by $E_n = B + Cexp(D/T)$; where the constants B, C, and D should be determined experimentally. The coefficient B can be embedded into η_0, and after taking the logarithm of Eq. 3.2, Arrhenius gives the empirical viscosity relation for chalcogenide glasses as in Eq. 3.3 where the coefficients has specific values for different glasses [56];

$$\log(\eta) = \log(\eta_0) + \left(\frac{C \exp(D/T)}{2.3RT} \right) \tag{3.3}$$

A recent study on the fiber drawing with As_2Se_3 gives a similar relation for the viscosity relation of As_2Se_3 in Eq. 3.4 using Vogel-Fulcher-Tamman formulation [57, 58]. In this formulation constants vary with the composition of glass. A comparison of these two models along with the experimental data are given in Fig. 3.4 where the constants for As_2Se_3 are given in Table 3.1. As it is seen from

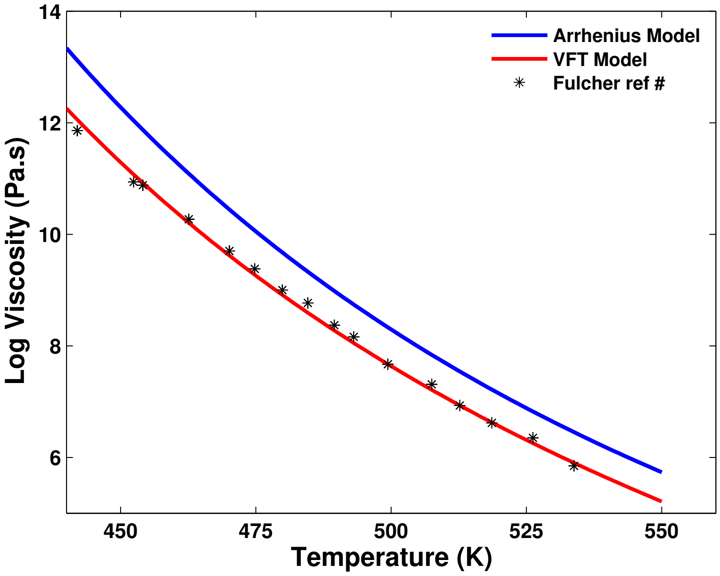

Figure 3.4: The comparison of Arrhenius and Vogel-Fulcher-Tamman models on the viscosity data (Fulcher, 1925) of As_2Se_3.

Table 3.1: Coefficients used to calculate the plot in Fig. 3.4.

Arrhenius Model [56]		Vogel-Fulcher-Tamman Model [58]	
$\log \eta_0$	-3.09	A	6.79
C	18878	B	3569.20
D	876	T_0	252.60

the figure Vogel-Fulcher-Tamman model gives smaller error assuming the data is very close to real values.

$$\log(\eta) = -A + \left(\frac{B}{T - T_0}\right) \tag{3.4}$$

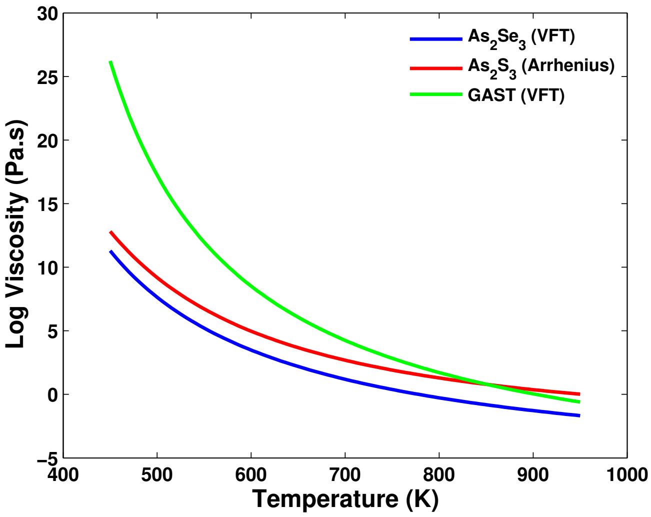

Figure 3.5: Viscosity behaviors of candidate chalcogenide materials.

For As_2S_3, there is not any study on the Vogel-Fulcher-Tamman model. Hence, in this thesis we will use Arrhenius model for this glass with the coefficients: $\log\eta_0$=-3.62, C=33744.1, D=650.8 [56]. For the Ge-As-Se-Te system, VFT model is reported on various compositions [59]. This study has shown that as the Te component decreases viscosity of the material also increases as explained above. The coefficients for the $Ge_{30}As_{13}Se_{27}Te_{30}$ are given as; A=8.1, B=4868 and T_0=308.52K [59]. Here, we will use these coefficients for comparison however actual viscosity values should be lower than this result. Fig. 3.5 illustrates viscosity behaviors of the three chalcogenide glasses.

Similar to the chalcogenide glasses viscosity of thermoplastics are estimated using similar formulations together with Trouton relation. The model proposed for the polymers is called Williams-Landel-Ferry Model (Eq. 3.5) [56]. Here, the coefficients are given as C_1=8.86 kJ/mol and C_2=52.86 K. T_r=T_g+43 K. The $\log\eta_0$ values are determined from the experimental measurements. Using fabrication parameters together with Trouton relation for the uniaxial direction (Eq. 3.6) we were able to calculate specific viscosity values for PES and PEI. The change in strain is directly related to the change in volume of the preform and the produced fiber. Hence, the preform feed speed and fiber drawing speed gives exact value of change in strain; $\frac{d\epsilon}{dt} = \frac{\nu - V}{\nu}$. Using this relation, we measured viscosity of PES as 5.14×10^4 $Pa \cdot s$ at 289 °C (562 K) and viscosity of PEI as 1.19×10^5 $Pa \cdot s$ at 295 °C (568 K). Using this value and Williams-Landel-Ferry equation (Eq. 3.5) η_0 values are found as 1.99×10^8 $Pa \cdot s$ for PES and 1.39×10^9 $Pa \cdot s$ for PEI. Table 3.2 gives these values together with $\log \eta_0$, T$_r$ values and Fig. 3.6 gives calculated viscosity-temperature dependence of candidate thermoplastics.

$$\log(\eta) = \log(\eta_0) + \left(\frac{-C_1(T - T_r)}{C_2 + T - T_r} \right) \tag{3.5}$$

$$\sigma_z = 3\eta_0 \frac{d\epsilon_z}{dt} \tag{3.6}$$

Table 3.2: Calculated parameters of PES and PEI for the Williams-Landel-Ferry viscosity calculation model. Here, $d\epsilon/dt = (\nu - V)/\nu$ where ν is fiber drawing speed and V is feed speed in m/s.

PES		PEI	
ν (at 562K)	0.007 m/s	ν (at 568K)	0.0035 m/s
V (at 562K)	1.50×10^{-5} m/s	V (at 568K)	0.87×10^{-5} m/s
$\log \eta_0$	8.268 $Pa \cdot s$	$\log \eta_0$	8.601 $Pa \cdot s$
T_g	493 K	T_g	490 K
T_r	526 K	T_r	523 K

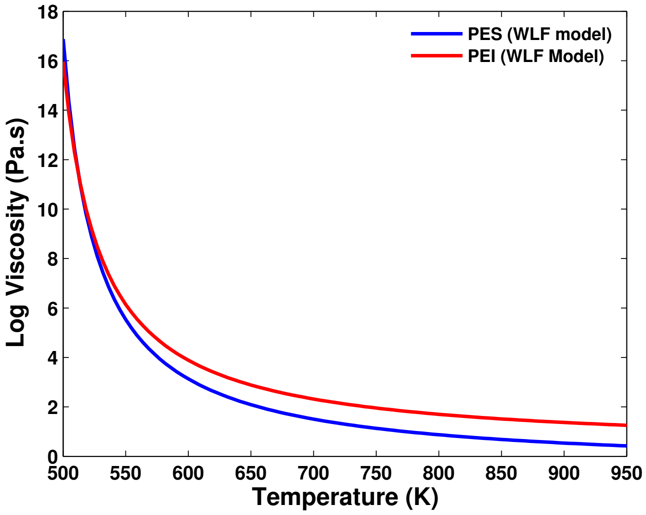

Figure 3.6: The viscosity behaviors of polymers PES and PEI.

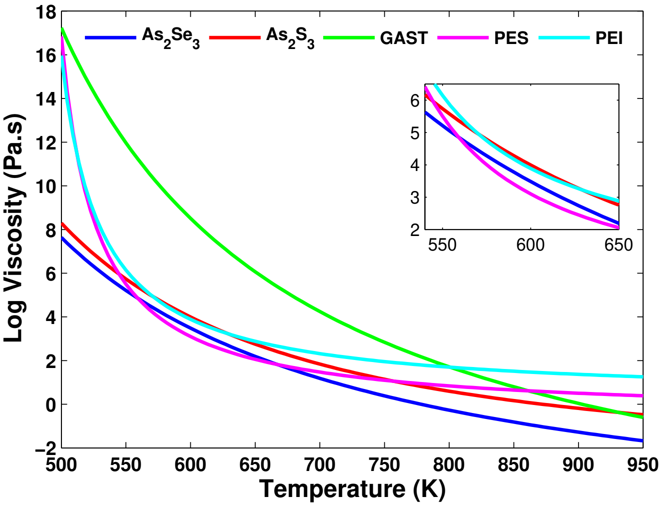

Figure 3.7: The temperature viscosity dependence of the candidate material calculated using different models. The inset gives a close look to the region where all materials except GAST has close viscosity values.

Fig. 3.7 gives a complete comparison of viscosities of all candidate materials. As it is seen in the figure GAST glass has fairly different viscosity behavior than the others. Hence, at this point we eliminated GAST as a candidate material. For the remaining materials the optimum temperatures are ranging from 540-600 K (267-327 °C).

An important phenomena that should be considered for the design and fabrication process is the capillary break-up limit for glass layers. First trials of the fiber fabrication showed that for the outer layers of chalcogenide glasses capillary break is very common(The fabrication process will be explained in detail in the next section). This means that there is a limit for the chalcogenide layers and hence there is limit for highest frequency transmitted by the fiber. This layer thickness limit is reported for As_2Se_3 as around 200 nm [12, 45]. Necessary layer thicknesses for the same glass will be calculated in the following section. However, studies have shown that it is possible to fabricate well functioning fibers with band gaps around 2-3 μm which require glass thicknesses around 200-250 nm.

Thermal fiber drawing process is done at fairly high temperatures and fabrication of composite fiber structure requires materials to have similar thermomechanical properties. First of all, materials should have high crystallization temperatures and close glass transition temperatures. That enables them to have similar viscosity-temperature dependencies for a particular range. We have shown that using semi-empirical calculation, all of our materials have similar viscosity values for 540-600 K, except GAST glass which has higher viscosity values compared to other glasses. Still, studies have shown that it is possible to fabricate composite fibers containing small percentages of GAST glass [15]. However, we will not use GAST glass for the fabrication of high power laser delivery fibers.

In conclusion two chalcogenide glasses (As_2Se_3 and As_2S_3) and two polymers (PES and PEI) have similar thermomechanical properties and can easily be considered in the fabrication of photonic band gap fibers using thermal drawing process.

3.1.2 Optical Properties

Optical properties of materials have great importance for the function of end product since optical band gap is mostly depend on these properties. Hence, an optical characterization should be done for both choosing materials with lowest losses at the operating wavelengths and adjusting fabrication parameters. Using optical data of materials it is possible to calculate necessary film thicknesses for different wavelengths. However, this thesis will focus on specific laser beam deliveries for medical surgeries. Main focus of this thesis is fabrication of PBG fibers for CO_2 laser beam delivery. Hence, we will design out whole process considering the operating wavelength of CO_2 laser which is 10.6 μm.

The first step for the optical characterization is to determine dispersion relation of the materials. For this purpose a J.A. Woollam IR-Vase Ellipsometer is used to acquire ellipsometric optical data of the materials. Materials are deposited on crystal silicon substrates for certain thicknesses for measurements. Then ellipsometric data is fit to Cauchy function which is given in Eq. 3.7 [60, 61].

$$nk = \frac{1}{2}\epsilon_i = \frac{a_j}{(\omega - \omega_j)^2 + b_j^2} \tag{3.7}$$

where, n is refractive index; k is the absorption index; ϵ_i is the imaginary dielectric constant; a_j/b_j^2 is peak height at the resonance frequency; ω_j is the resonance frequency; and $2b_j$ is the width of half maximum at the resonance frequency. Eq. 3.7 basically gives the Kramers-Kronig relation between real and imaginary components of the dielectric constant casted into Cauchy formulation. A more convenient formulation is used by the ellipsometry system (Eq. 3.8) with the coefficients are determined via fitting the reflection signals of ordinary and extraordinary oriented light rays [62]. The results of measurements and fitting calculations are given in Fig. 3.8.

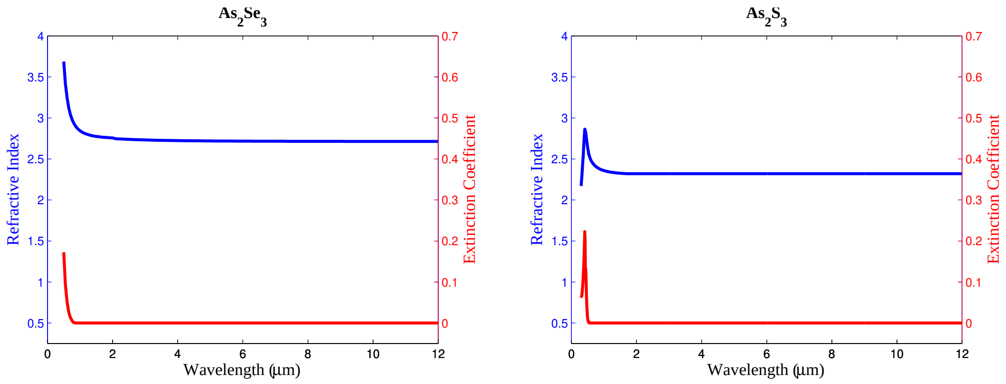

(a) Arsenic triselenide

(b) Arsenic trisulfide

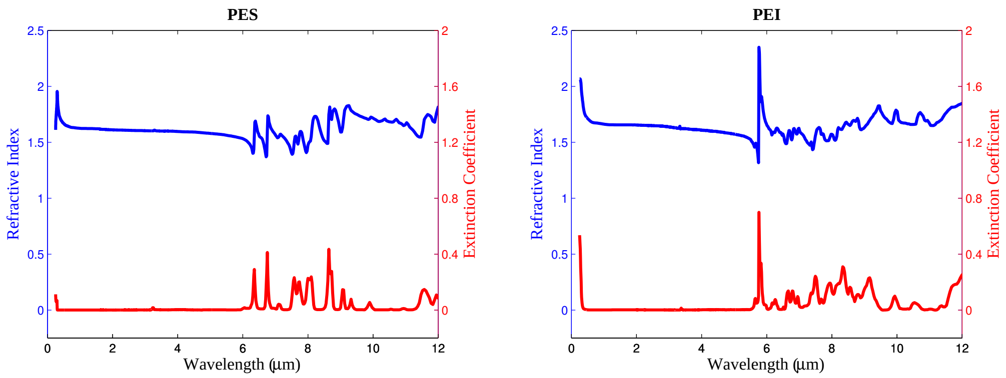

(c) Poly (ether sulfone)

(d) Poly (ether imide)

Figure 3.8: Dispersion relations of candidate materials.

$$\begin{aligned} n(\lambda) &= A + \frac{B}{\lambda^2} + \frac{C}{\lambda^4} \\ k(\lambda) &= \beta \exp\left[\gamma\left(\frac{1}{\lambda} - \frac{1}{L}\right)\right] \end{aligned} \tag{3.8}$$

In Chapter 2, the necessity of high refractive index contrast is mentioned. High refractive index contrast is an important criteria when choosing glass-polymer material set. According to the measurements the refractive index of As_2Se_3 is about 2.75 and of As_2S_3 is about 2.30 around 10.6 μm. Refractive index of polymers are very close around 10.6 μm, however it can be seen from the figure that polymers have higher absorption values around the wavelength of concern. Extinction coefficient of PES is lower compared to PEI. Thus, PES is a better candidate for the fabrication of PBG fiber for CO_2 laser delivery.

In summary, after a detailed examination of materials' thermomechanical and optical properties best material set for the fabrication of dielectric Bragg fibers for guiding around mid-IR region is As_2Se_3 - PES glass-polymer system. Further material properties specifically related to the fabrication steps and overall fabrication process will explained in the following chapter.

3.2 Fiber Design

Theoretical background of optical band gap and required properties for an efficient light guiding is explained in Chapter 2. In the previous section, other properties of materials are examined for the fabrication process and based on the measurements best material set for CO_2 laser beam delivery is found as As_2Se_3 - PES system. In this section, having all the properties of these materials we will focus on the design of the preform from which PBG fibers will be drawn.

A preform is basically a macro object which has the same structure with the resultant fiber by a factor. In order to draw fibers from a multi-material preform, thermomechanical properties of the materials must be similar. We have explained that both As_2Se_3 and PES close softening points i.e. similar viscosity values for the range 267-327 °C. Additionally, both of the materials have close thermal expansion values. Other common properties of these materials are given in Table 3.3.

Table 3.3: General properties of As_2Se_3 and PES. The data are taken from, Amorphous Materials Inc., Glassy Semiconductors [54] and Properties of Polymers [50].

Property	As_2Se_3	PES
Glass Transition Temperature	190 °C	220 °C
Softening Point	~200 °C	226 °C
Thermal Expansion	22.4×10^{-6} /°C	52×10^{-6} /°C
Refractive index at 10.6μm	2.75	1.65
Density	4.69 gm/cm^3	1.37 gm/cm^3

In the preceding chapter common light guiding mechanisms in the fibers are explained. Conventional optical fibers guide light through a solid core by total internal reflections on the interface of the core and cladding. The novel fiber structures generally use air guiding mechanisms to eliminate material non-linearities and absorptions. However, in order to light guiding in air there should be optical band gap along the radial direction of the fiber. In fiber geometry optical band gap can be created by both one- or two- dimensional symmetric structures. In Chapter 2 we have shown that is possible to construct 1D multilayered dielectric mirror with omnidirectional reflectivity. Together with the material characteristics fabricating a fiber with 1D mirror structures on the inner surface is the smart choice for our purpose. Thus, in this section design of preform structures for the fabrication of 1D PBG fibers is explained.

Constructing a cylindrical preform with multilayered structure on the inside is an important step for the whole fabrication process. In this study chalcogenide glasses are purchased in bulk from Amorphous Materials Inc. (commercial names of As_2Se_3 is Amtir-2 and of As_2S_3 is Amtir-3) and the polymers are obtained in the film form from Ajedium with names Ultem (PEI) and Ultrason E (PES). Films are purchased with different thicknesses (10, 50, 100 μm) and in order to have a multilayered structure chalcogenide materials should be deposited onto the PES film. For omnidirectional reflectivity there should be a frequency dependent ratio between the layer thicknesses of dielectric material (Eq. 2.1). Accordingly, the macro form of the fiber should also have this ratio which gives the thickness of deposited chalcogenide glass and this ratio should be preserved during the fiber drawing process. If the materials have nearly constant refractive index values for a range of frequency, this ratio enables fabrication PBG fibers, which transmits light for a particular frequency in the range, just by changing the reduction factor between the preform diameter and the fiber diameter. Hence, with the same material set it is possible to produce different PBG fibers with different operating wavelengths.

CO_2 laser is a gas laser which produces a laser beam centered around 10.6 μm wavelength; so that optical band formed by the multilayered structure must be around this wavelength. Refractive indices of As_2Se_3 and PES around 10.6 μm are 2.71 and 1.68 respectively. According to QWS formulation, their thicknesses should be inversely proportional to their refractive indices. Thence, their thickness ratio must be $d_1/d_2 = n_2/n_1$ where 1 and 2 refers to As_2Se_3 and PES. Table 3.4 gives the thickness ratio and required layer thicknesses of the materials.

Table 3.4: Structure parameters of the materials for both fiber and preform.

Material	Refractive Index @ 10.6 μm	Thickness Ratio (d_1/d_2)	Layer Thickness in fiber	Layer Thickness in preform
As_2Se_3	2.75	0.6	0.98 μm	30 μm
PES	1.65		1.58 μm	50 μm

The aimed size of the fiber and the preform are determined using optical parameters of the materials. Before going further into the process steps, we should check the calculated reflection and band diagram of the 1D dielectric mirror that we want on the inner surface of the fiber. Fig. 3.9(a) is the band diagram of a one dimensional mirror which is made 10 pairs of As_2Se_3 and PES. The thickness ration is 0.6. As it is seen from the figure this structure has a complete band for all incidence angles for a frequency range.

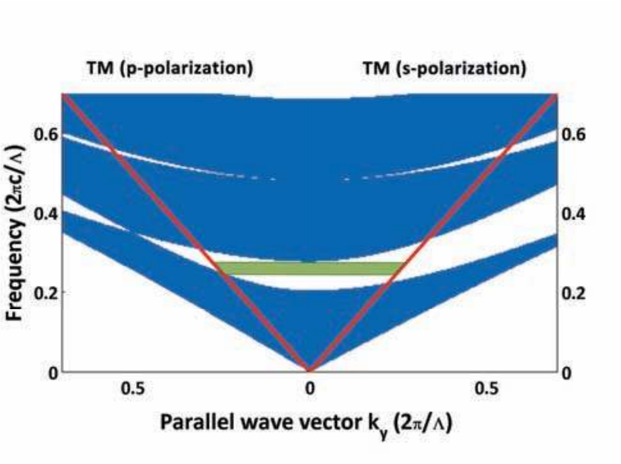

(a) Band Diagram

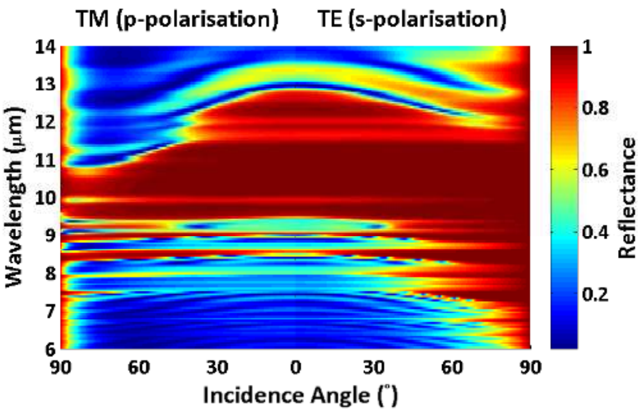

(b) Reflectance - Angle Dependence

Figure 3.9: (a) Band diagram of a 10 pair As_2Se_3-PES dielectric mirror without losses. (b) Calculated reflectance profile of the same mirror with included dispersion.

In this extend the band gap of the mirror can be shifted by changing the pitch size which is the sum of two thicknesses. Fig. 3.9(a) is calculated assuming there is not any loss and the index of the material is constant through the frequency range. Fig. 3.9(b) is, on the other hand, an angle dependent reflectance response of the same mirror with dispersions of the materials are included. We can see that there is an optical bad for all angles around 10.6 μm except the reflectance is decreased at 9.8 μm wavelength since PES has an absorption peak around this wavelength. Thus, we are expecting a dip in the transmission of the produced fiber near 9.8 μm.

3.3 Thin Film Production

Fabrication of high power laser delivery fibers requires some basic steps before the production process. These steps are materials selection criteria and materials characterization, and design of fiber using optical properties and basic theories. Starting from this section we will look at fabrication steps which are, film deposition, preform preparation, and thermal drawing. The first step of the process, film deposition requires a special attention since the structure of the film is very crucial to have a well functioning optical band gap.

In order to have a multilayered structure, one can conclude that these materials should be formed in film geometry. As stated above PES is commercially in film form and As_2Se_3 in bulk form. Thence, the clever way to form these materials is to deposit chalcogenide glass onto the polymer film. There are a number of ways to deposit As_2Se_3 onto PES films. One of these methods are thermal evaporation of glass material. It is simply evaporating a solid material in a vacuum chamber and deposition on a substrate. Although this is a simple method, one should consider if there is any change in the stoichiometry of the material. A second way is sputtering in which highly energetic inert gas ions are collided to the target material to free the molecules from the target. Subsequently the liberated particles are deposited on a substrate. This process requires low temperatures; however the deposition rate is very low compared to thermal evaporation. Other methods for the deposition are e-beam evaporation and chemical vapor deposition. Nevertheless these methods are complicated and require expensive experimental setup.

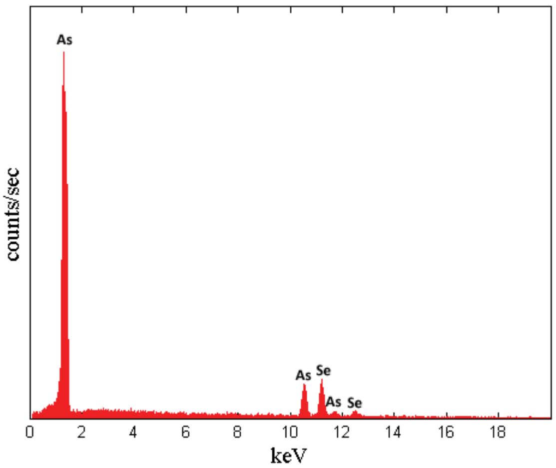

Figure 3.10: EDX analysis of coated As_2Se_3.

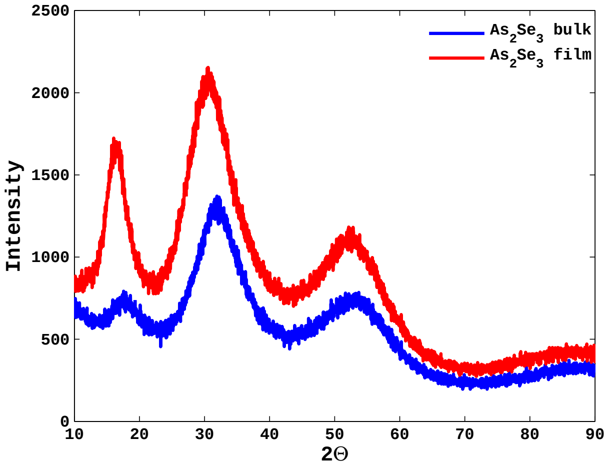

Figure 3.11: X-Ray diffraction measurements of bulk powdered As_2Se_3 and film As_2Se_3.

The method used for the film deposition in this study is thermal evaporation. In the following section details of the evaporating system and the optimization steps will be explained. Thermal evaporation is the most convenient method since the system is not complex and the deposition rate is high which is an important factor for the future of this study in a time manner. However, since we are evaporating the chalcogenide glass and deposit again on a polymer substrate, stoichiometry of the glass should be checked before and after the depositions. This stoichiometric measurements are done via FEI Nova 600i Nanolab model energy dispersive X-ray spectroscopy (Fig. 3.10). Measurements showed that after evaporation of As_2Se_3 at% of As is 45% and of Se is 55%. This means that the atomic ratio of the glass is mostly preserved during thermal evaporation. Another important property that should be considered is the structure of the glass. Since, the chalcogenide film will experience a series of thermal processes, it should remain amorphous after the evaporation process. Fig. 3.11 is the X-Ray diffraction results of powder As_2Se_3 and film formed As_2Se_3. The film is deposited using a physical vapor deposition system. As it is seen from the figure amorphous structure of the glass is preserved during the evaporation process and no crystallization is observed. Hence, use of As_2Se_3 chalcogenide glass and use of thermal evaporation process is a promising method for the ultimate purpose of this study.

3.3.1 Thin Film Coating System

The review of different deposition techniques that can be used for the chalcogenide film formation is given in the previous section. As explained above the best choice for this process is thermal evaporation because of both the low costs, high deposition rate and ease of the technique. In this step of the fabrication, polymer film is used as a substrate and glass is used as the deposited material. Hence, this glass coated polymer can be formed into a roll which has consecutive layers of chalcogenide glass and thermoplastic. For this purpose a large area coated polymer film is required which is a troubling challenge for the construction of the thermal evaporation system.

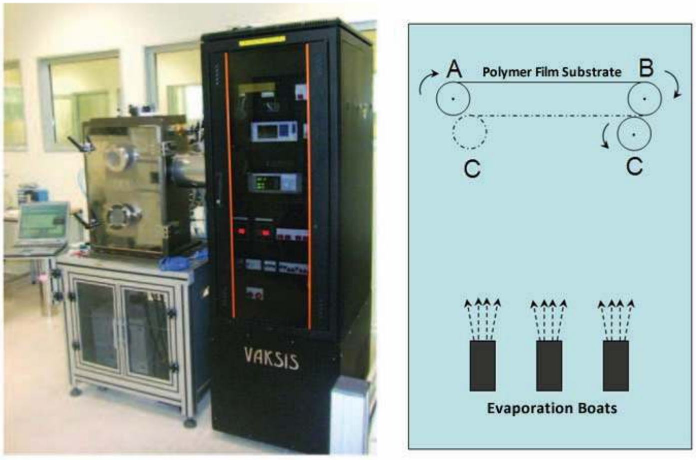

Figure 3.12: A general look of custom designed thermal evaporator system (Elif) and schematic diagram of first designed system.

The main concern here is to have uniformly coated glass layer through the whole polymer film. In order to fulfill this purpose a custom designed thermal evaporation system named Elif is built by Vaksis Corp. (Fig. 3.12). However, experiments have shown that the first design of the evaporator was not suitable to have uniformly coated stable glass films since the polymer film handling of the system was not matching the quality required. Therefore a system upgrade is employed in order to make film handling better. The second design for the system is given in Fig. 3.13. This design gave good film qualities by which we were able to draw PBG fibers with the desired micro structure. Using this system we were able to coat 22 cm×75 cm polymer film with thicknesses ranging from 13 to 15 μm along the film.

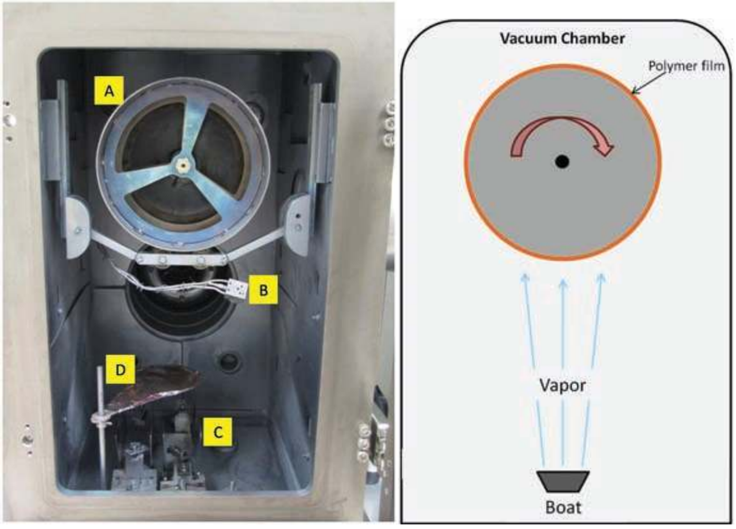

Figure 3.13: (a) Second version of Elif evaporation system. Here the letters are; A: The big cylinder on which substrate polymer film is wrapped and fixed; B: Thickness monitor; C: Boats; D:The shutter which enables a sudden stop of coating. (b) The schematic diagram of upgraded coating system.

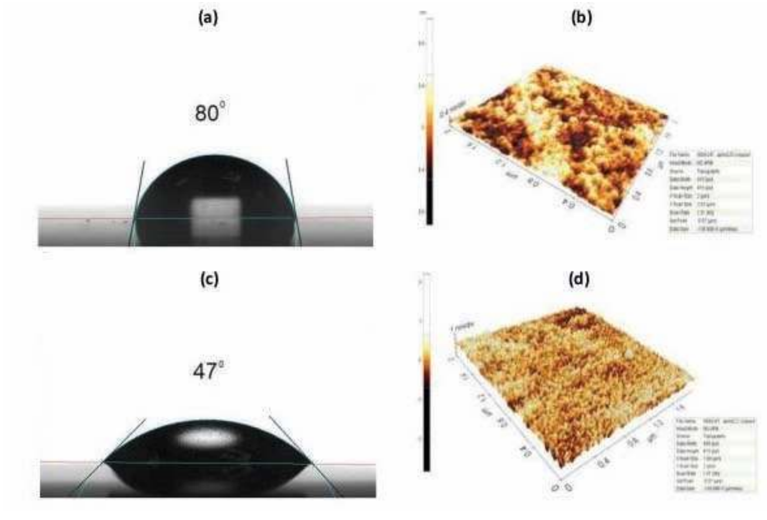

Figure 3.14: The contact angle measurements and AFM images of regular (a,b) and plasma treated (c,d) polymers. Microwave operating frequency 2.4 GHz and the power is about 100 W for five minutes [63].

During evaporation process adhesion of the materials onto each other is an important parameter for the physical integrity of the film. Contact angle experiments can be employed in order to measure this property. However, since softening points of these materials are both high and close to each other, using water drop is a much easier method to see the surface energy of the films and coating. In order to increase surface roughness for increasing glass adhesion to the polymer, a high energy plasma etching methods is used. For this purpose an argon rich environment is provided inside the evaporation chamber and a microwave source for the ionization of inert gas is used. Fig. 3.14 is a previous study on the plasma etching on a PES film [63]. It can be concluded that plasma etching process increases material adhesion between As_2Se_3 and PES.

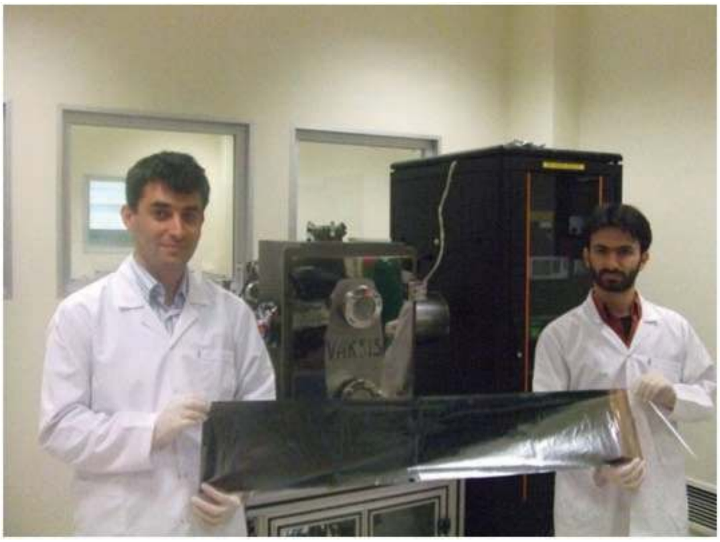

Figure 3.15: A photograph of large are coated polymer film.

In the Fiber Design section we calculated the ratio between the layer thicknesses as 0.6 using QWS formulation. Hence, during the glass coating on polymer this ratio should be conserved. One thing to keep in mind is we are coating both sides of the polymer film because 0.6 is a fairly high ratio for a stable film formation on the polymer. Hence, instead of coating all the glass on one surface of the polymer we coated both sides of the film with the half of aimed glass thickness. We have PES polymers with three different thicknesses; 10, 50 and 100 μm. Our studies have shown that the optimum film thickness used as a substrate is 50 μm-thick film since 10 μm is very thin and too hard to handle, and 100 μm-thick film needs about 60 μm thick glass coating which need very long coating time and excess amount of glass material. Thence, a 24 cm×75 cm×50 μm film is used as a substrate and coated with As_2Se_3 with an average coating rate of 2 nm/sec. Fig. 3.15 is an image of large area coated 50 μm-thick PES polymer with As_2Se_3 coating material.

3.3.2 Uniformity Calculations

As stated above using this geometry we were able to coat large area polymers; but due to film uniformity this system also needed further development. Basic objective of the system development is to increase the uniformity of the film. The importance of the film uniformity arises from having a constant thickness ratio along the whole preform and having same optical properties for both fiber drawn from the beginning of the preform or somewhere in the middle. Hence, uniformity calculations become crucial for our system since the vapor of the material outspread in the hemisphere with a cosine exponent. The point on the film which is directly above the source experiences much more vapor than the point that has an offset from the point of source.

The uniformity of the coated film can be calculated using maximum and minimum film thicknesses by using Eq. 3.9. For the prediction of the film thicknesses one can use the vapor distribution of the melted material through the substrate surface. In the ideal case the distribution of the vapor should have a half-spherical shape (isotropic). However, due to many effects, like the evaporation rate of the material, the temperature of the chamber and the shape of the source, this is not the case in laboratory environment. Eq. 3.10 gives normalized thickness of a point on a rotating substrate with t_0 is the thickness of the film on the point of rotation [64, 65]. However, in our system the cylinder rotates around an axis that is parallel to the PES film surface. Geometry of the evaporator and parameters of the equation are both represented in Fig. 3.16. Thus, when we reduce the equation for a stationary substrate we have Eq. 3.11;

$$\nu = 100 \times \frac{t_{max} - t_{min}}{t_{max} + t_{min}} \tag{3.9}$$

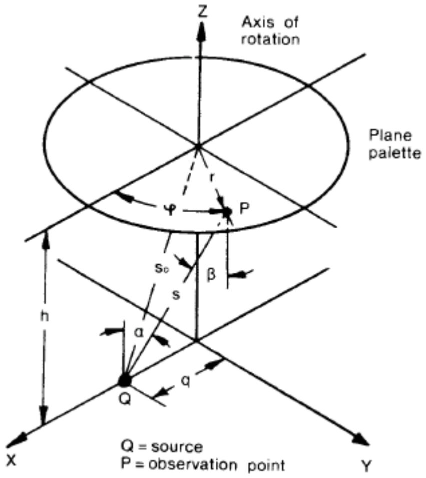

Figure 3.16: Evaporator geometry with a plane palette as a substrate holder. Adapted from [65].

$$\frac{t}{t_0} = \left[1 + \left(\frac{q}{h}\right)^2\right]^{(n+3)/2} \frac{1}{\pi} \int_0^{pi} \frac{\mathrm{d}\phi}{\left[1 + \left(\frac{r}{h}\right)^2 + \left(\frac{q}{h}\right)^2 - \left(\frac{2r}{h}\right)\left(\frac{q}{h}\right)^2 \cos\phi\right]^{(n+3)/2}} \tag{3.10}$$

$$\frac{t}{t_0} = \left[\frac{h^2 + q^2}{h^2 + (q-r)^2}\right]^{(n+3)/2} \tag{3.11}$$

For the calculated uniformity profiles we implemented a MATLAB code that is using Eq. 3.11. Our calculations have indicated that, there are certain parameters that we can change in our evaporator. For instance, changing the size of the boat will add up to the thickness for each point. We can use boat size as one parameter. Another is the height of the substrate. However, due to the size of the vacuum chamber we have a limit in changing these parameters. The size of our vacuum chamber is 35 cm×35 cm×70 cm. Additionally, because of the initial design, maximum boat length we can use is 11cm. Hence, our calculations are done for the optimization of the boat size and height of the substrate film.

The exponent in the equation defines the vapor distribution profile of the evaporated materials. n=0 means that the vapor is spread in a isotropic manner that the vapor construct a perfect hemisphere. n=1 means a cosine distribution

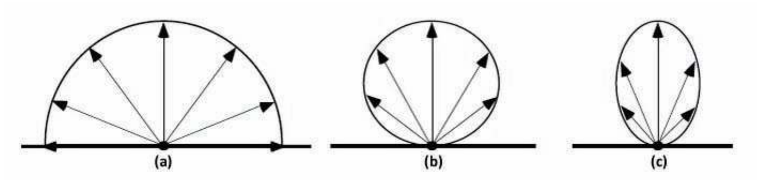

]

Figure 3.17: (a) Uniform emission from a point source (n=0); (b) Cosine emission from a small planar source (n=1); (c) Non-ideal, anisotropic emission from a small planar surface source (n>1).

along the space and n>1 means an anisotropic vapor emission from a small planar source (Fig. 3.17). This exponent is dependent on the evaporation system. Therefore, we calculated the exponent n of our system by fitting sample data to the theory. For the calculations we need dimensions of the vacuum chamber and relative positions of the big cylinder and source boats. These properties of the evaporation system are given in Fig. 3.18. Taking all the parameters into consideration, a theoretical fit is done to a coated PES film to determine the exponent of our system (Fig. 3.19). Our calculations indicates that the exponent of Elif evaporator is found as n=4 which is used as the value for the spread profile of the glass vapor in uniformity calculations.

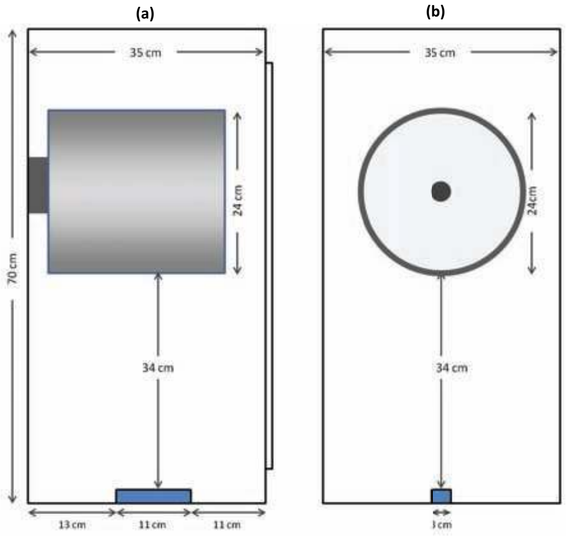

Figure 3.18: (a) Side view of the Elif evaporation system vacuum chamber. (b) Front view of the chamber.

The first parameter to consider to increase film uniformity is source size. Since our system is constraint to a upper limit of 11 cm boat size, we will compare two

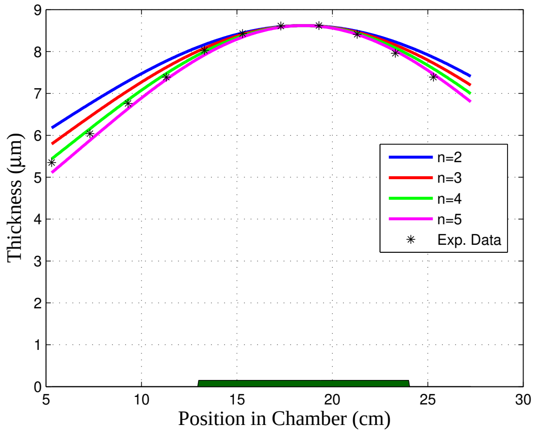

Figure 3.19: Theoretical thickness calculations of Elif evaporation system with different exponents and the experimental thickness values. The green filled area represents the place of the boat.

types of boats; 5 cm and 11 cm. Fig. 3.20 gives the result of this comparison. As

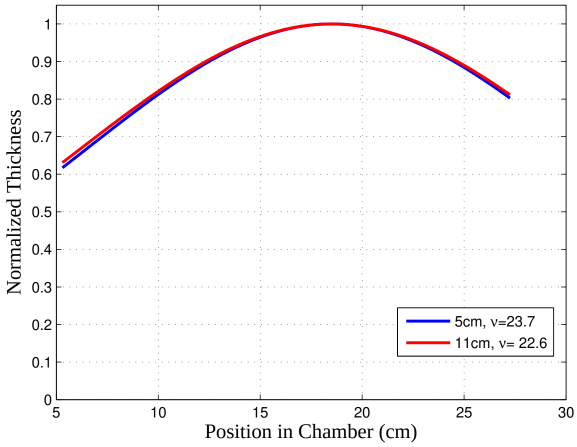

]

Figure 3.20: Calculated normalized thickness profile for boat sizes 5 cm and 11 cm.

it is seen from the figure, changing boat size does not have a considerable effect in the uniformity of the film. Uniformity for a 5cm boat is 23.7% whereas for 11 cm boat its value is 22.6%. Main reason is both of the sizes are small compared to film length. Therefore, as long as boat length is smaller than the substrate, the change in the uniformity will be very small. Taking the results of the calculations into account, we upgraded our boats to 11 cm boats with a uniformly distributed holes on the top. Our calculations showed that although uniformly distributed holes provide a well spread material vapor, it does not have any effect on the film uniformity.

The second parameter is more important than the boat size which is the height of the substrate. As it can be seen from Fig. 3.21, the farther the substrate gets in the vertical direction, the more uniform the film. Hence here again the limiting factor in the increase of the height is the size of the vacuum chamber. The diameter of the cylinder is about 24 cm which makes a PES film length of 75 cm. Hence, the maximum substrate height that we can reach with our system is about 35 cm. If the size of the cylinder is reduced the height of the substrate can be increased. For a highly efficient optical band gap the minimum film length is calculated as about 44 cm (will be explained in the following sections). This length corresponds to a cylinder diameter of 14 cm. Considering the size of the vacuum chamber we concluded that two identical cylinders with diameter 14 cm can be placed into the chamber. In this case the height of the cylinders is 48.5 cm from the boat level and the distance between the boat and the closest point of the cylinder becomes 49 cm. The scheme of the new designed system is in Fig. 3.22. Both theoretical uniformity calculations and experimental data showed that with 2-cylinder system there is a considerable improvement in the film uniformity (Fig. 3.23).

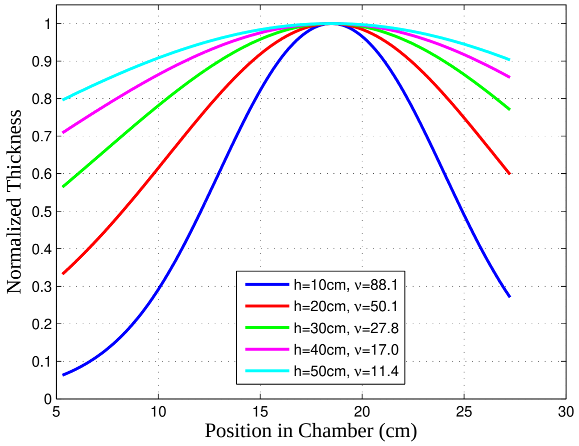

]

Figure 3.21: Calculated normalized thickness profile for different substrate heights. As the height of the substrate increases the film uniformity decreases.

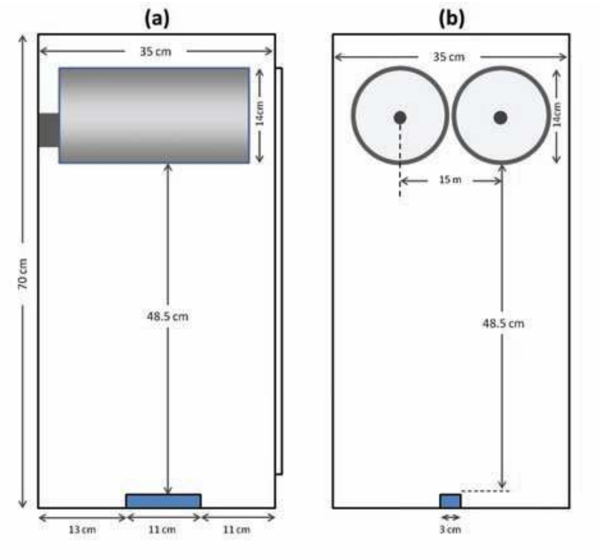

Figure 3.22: (a) Side view of the newly designed Elif evaporation system vacuum chamber. (b) Front view of the chamber.

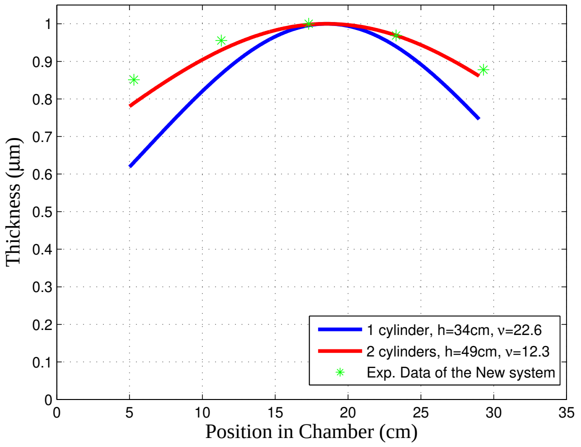

Figure 3.23: Comparison of uniformity of films coated in 1-cylinder and 2-cylinder evaporation systems. The green represents the measured film thicknesses of a PES film coated in the new, 2-cylinder system.

Figure 3.24: Picture of upgraded Elif evaporator system.

Calculations and measurements resulted in an improvement in the uniformity with the use of new 2-cylinder coating system (Fig. 3.24). Therefore we revised our system and transferred the motor motion to the cylinders with a mechanical chain. Main difference is the increase in distance between the source and the substrate.

3.3.3 Film Characterization

3.3.3.1 Thickness Measurements

Film thickness measurement is an important step for both the enhancement of the production process and determining the drawing parameters in order to get a PBG fiber functioning around 10.6 μm. The challenges for the thickness measurements are having very large samples and thickness values for the conventional thickness measurement equipments. For this purpose, we used a simple method to measure the thickness of the film. Basically the method used by conventional ellipsometers. We employed same idea to simple reflection response of materials measured by FTIR systems. The system used in our study is Thermo Scientific Nicolet 6700 model FTIR system. After getting spectral reflection from the coated film, we used TMM method and optical properties of the materials to get the theoretical reflection. By fitting this reflection to the measured response of the film and having the fact that the thickness is the adjustable parameter for the theoretical calculation, we were able to measure the thickness of the film.

Data fitting can be done by usual computational software programs. For this purpose we used Mathematica 6.0 and the thickness spanning was done easily by the *Manipulate* tool of this program. The figure below is an image of a typical thickness measurements fitting program (Fig. 3.25). The red dotted lines are interferometric reflection data of the film. The blue line is the theoretical model of the reflection which is changing with the thickness of the modeled film. Thus, the measurement of the film thickness is done half by experimental equipment and half theoretical modeling.

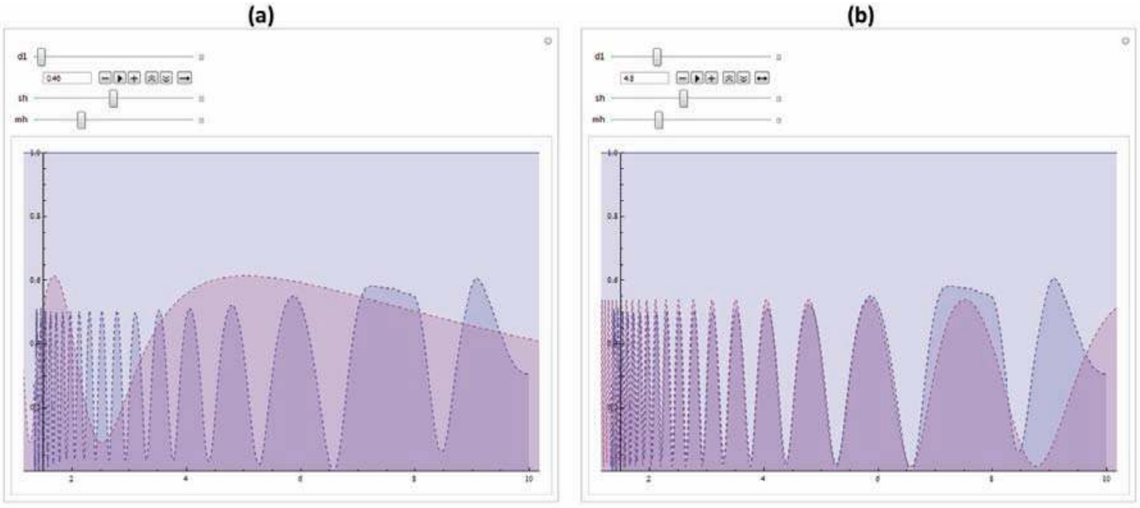

Figure 3.25: The program used for thickness measurement. Program is coded in Mathematica. The blue line is the interferometric reflection of the film and the red line is calculation result of TMM for one layer of As_2Se_3 on PES polymer. (a) The data and the calculation are unfitted. (b) The data and the calculation are fitted. *sh* and *mh* are shifting and and scaling parameters to make a good fit.

The reflection data of the film can change if the substrate effects are high. In interferometric reflection response the substrate effects becomes important when the thickness of the substrate is small i.e. there is an additional coherent layer. However, in this study the thickness of the substrate polymer film is 50 μm which is big enough to consider as a incoherent layer. It is still possible to measure thicknesses of multiple layers using this methods if the optical properties of the materials are known.

3.3.3.2 Film Surface

In the fiber structure very small difference on the surface can lead to scattering losses in the transmission of high power laser through the fiber. Hence, roughness on the coated film should be checked for the sake of the all process. A simple way to decrease roughness is to anneal coated films close to their softening points. In the previous sections we reported that as the temperature gets close to the softening point viscosity of the glass decreases and consequently due to surface tension effects the surface of the films gets smoother. However, one should consider that since the glass transition temperatures of PES and As_2Se_3 are close to each other annealing temperature should be chosen wisely. Fig. 3.26 gives AFM images of As_2Se_3 films as-coated and annealed at 180 °C for one day. Although it is not noteworthy, a decrease in the roughness can be observed. Additionally, during the drawing process, the feature size of the preform is decreasing for about 20-30 times. Hence, an average roughness of 5nm on the film surface means an average roughness of 0.25 nm in the fiber. Therefore, the advantage of film annealing is an open debate for the fabrication of PBG fibers.

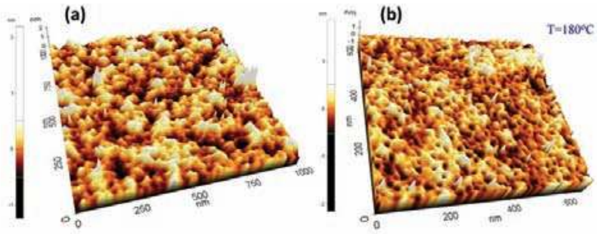

Figure 3.26: AFM images of As_2Se_3 films coated on SiO_2, before (a) and after (b) annealing.

3.4 Preform Preparation

The film coating process and optimizations to both the process and the equipment is explained in the preceding section. Preform preparation can be considered as the second major step of the fiber fabrication process. Preform is the macro structure of the fiber and is reduced to fiber during the drawing process. As explained above there is a certain ratio between glass and polymer films. Hence, when we are preparing the preform this should be the main concern. Additionally, the overall integrity of the preform should be provided through a consolidation process which is also a thermal treating process.

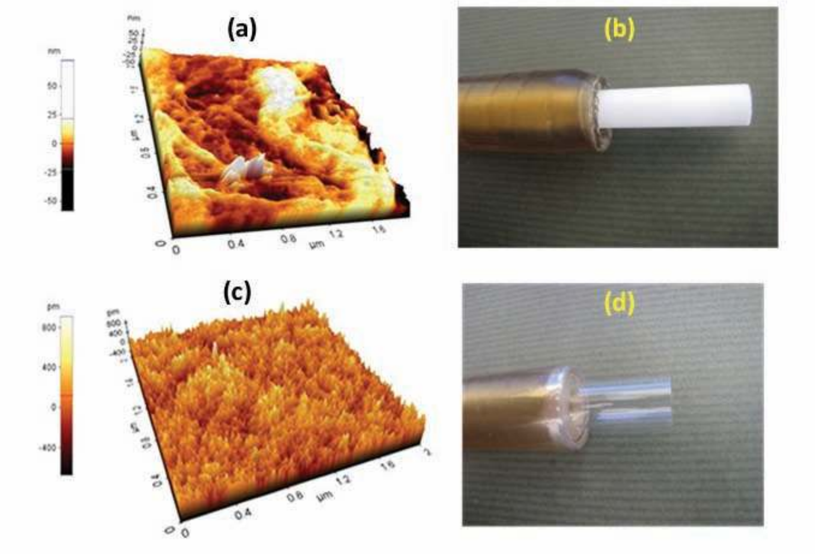

Figure 3.27: AFM images of PTFE and glass tubes together with images of consolidated preforms. The roughness of PTFE tube is on the 50 nm level whereas the roughness of glass is on the pm level.

Wrapping coated PES film onto a mold object for the layers of dielectric mirror is the beginning of the preform formation. This object is a temporary object and used to form the hollow core structure of the preform. Hence, after consolidation step we should get rid of this mold. This is one of the criteria in choosing the mold material. One can easily conclude that the surface properties of the mold material will be transformed to the inner surface of the preform. Thus, lower surface roughness is an desirable property. There are two candidates as mold; one this Teflon (polytetrafluoroethylene, PTFE) and other is glass tubes. Thermal coefficient of PTFE is 180×10^{-6} /°C which is high compared to our candidate materials. This property enables easy separation of the preform and the tube after the whole process since as the preform gets colder the radius of the tube will decrease with higher percentage. Additionally, candidate materials do not adhere to PTFE which enables conserving inner surface of preform during the separation. For glass, on the other hand, thermal expansion coefficient is 8.5×10^{-6} /°C i.e. size change of glass under thermal treatments is very small. This can be considered both as an advantage or disadvantage. Since the radius of the tube does not get bigger during the consolidation the arrangement of layers will not be affected. However, when we think about adhesion of materials to glass, we face a problem. Chalcogenides strongly adheres to silica glass and this makes mechanical separation impossible. Nevertheless, studies have shown that both PES and As_2Se_3 are unaffected from hydrofluoric acid (HF). Hence, HF can be used to etch glass tube even though this process needs additional time. Measurements indicated that there is a big difference in the roughnesses of PTFE and glass tube. AFM images are given in Fig. 3.27a and 3.27c; measured roughnesses of tubes are around 20 nm for PTFE tube and 1-2 nm for glass tube. Taking all the comparisons into account, we concluded that the wise choice for the mold is glass tube.

The flow diagram of the preform preparation is given in Fig. 3.28. Initially, double side coated film is wrapped around a glass tube. The coated film has 15-50-15 μm As_2Se_3-PES-As_2Se_3 structure. Hence, macro structures dielectric mirror has layers of 30 μm As_2Se_3 and 50 μm PES. In Fiber Design section the desired layer thicknesses for the fiber is calculated as 0.98 μm for As_2Se_3 and 1.58 μm for PES. This means the mirror structure should reduce to fiber geometry by a factor of 30. After layered structure, for the cladding of the fiber 100 μm thick PES films are wrapped. We desire the final diameter of the fiber should be around 1.2-1.5 mm for easy handling. For this reason the wrapping of 100 μm thick polymer films is continued up to a preform diameter of 3.6 cm. Then the roll is again wrapped with Teflon band in order to preserve the structure of the preform during the consolidation process. After annealing in the vacuum

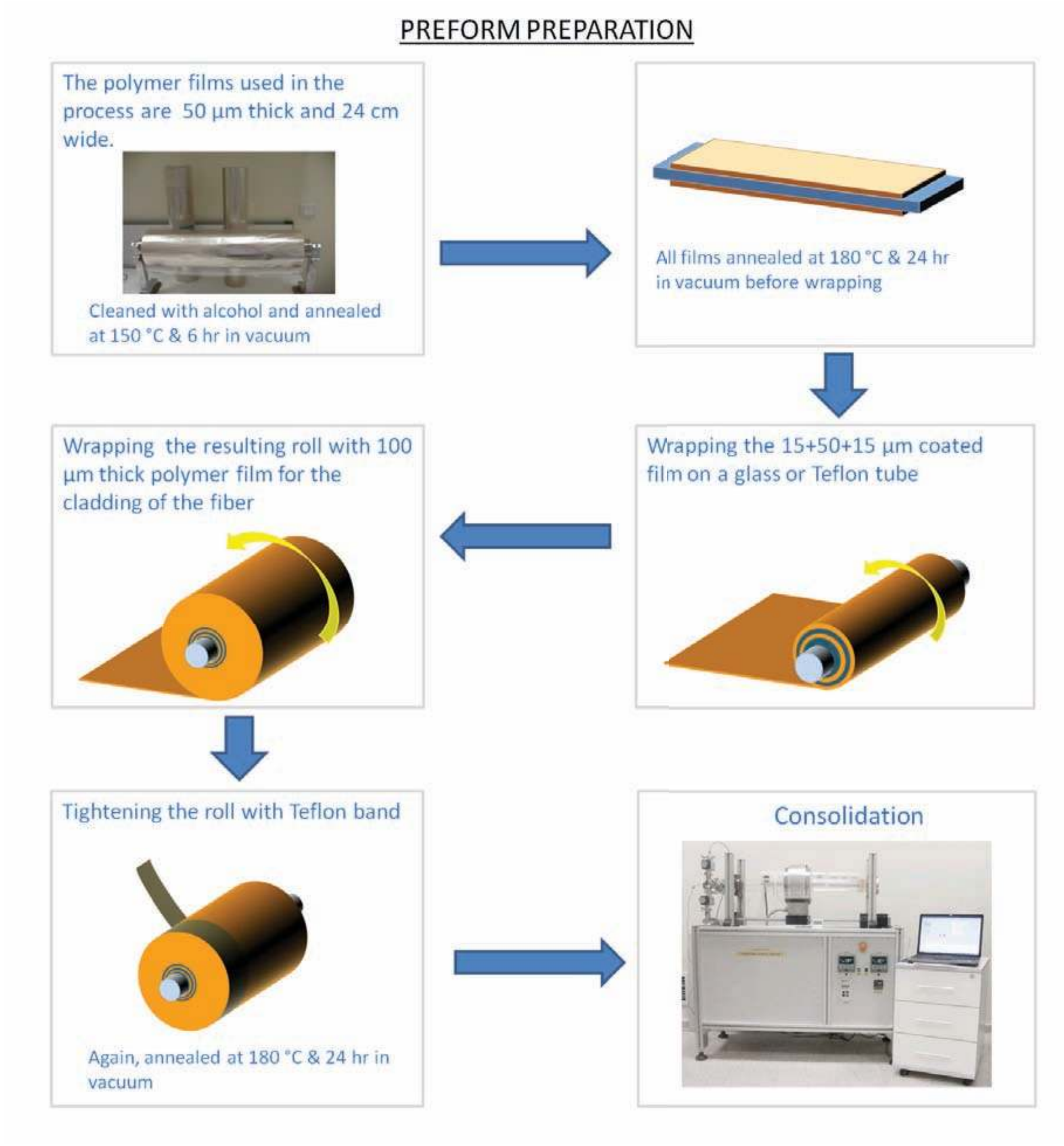

Figure 3.28: Flow diagram of preform preparation process.

chamber for one day the roll is consolidated in the custom built consolidation system (Fig. 3.29).

Figure 3.29: Custom built preform consolidator system.

Consolidation process is basically a heating process in low vacuum. After the wrapped roll is placed into the quartz tube, pressure is decreases to on the order of 10^{-2} Torr. Before the consolidation is done a preheating is done to eliminate trapped air between the layers of films. Preheating is done at 180 °C for 1 hour. The temperature is increased fast for this temperature (about 20 °C/min). Another advantage of preheating is reduction of temperature gradients and provide a controlled heating. After 1 hour, the temperature is increased to 257 °C with a rate of 2 °C/min. The rate is held at low level to provide a uniform heating though the preform. At 257 °C the polymer films are softens and merges to each other and the temperature is kept at this value for 35 minutes. At the end of this time, preform is immediately bring into the room condition and left to cool down. The last step is etching glass tube. For this purpose preform is left in the 48% HF acid for 3 hours. Trials have shown that, leaving preform for longer time period can result in deformation of As_2Se_3 layer on the inner surface of the preform and the optimum time for etching is between 2 h 45 min and 3

h. After glass etching and cleaning, preform is put in a vacuum chamber for demoisturization, etc. The next step is fiber drawing which will be explained in the following section.

3.5 Fiber Drawing

Thermal drawing is a very common fabrication method used mostly in the fabrication of conventional silica fibers. However, because the process does not specifically depend on basic characteristics of the material, different materials can be used for thermal drawing process with the appropriate fabrication parameters. Drawing is done at temperatures where the materials get soft and viscous. Hence, one can conclude that for fabrication of composite material fibers, thermoplastic properties of materials should be similar for some temperature range. In the previous sections it is shown that As_2Se_3 and PES has similar viscosity values for a temperature range 267-327 °C which also determines drawing temperature of the fiber.

Fiber tower used for fiber drawing is a custom built system together with its user interface (Fig. 3.30). Basic components of the tower are the micrometer movement systems, on stage measurement devices and two zone heating oven. The movement of the preform is done by x-y and z stages in order to provide axial alignment of the preform with the heating oven. Preform feeding is done by the z stage and fiber drawing speed is controlled by a capstan system. Adjusting the period of the capstan allow control of the fiber drawing speed and hence, diameter of the fiber. There are two real-time measurement systems in the tower. One is the laser micrometer which sends a simple laser beam and has a simple beam profiler. The difference in the profile of sent and received beam gives the diameter of the fiber. This measurement is done in two axis perpendicular to each other. Thus, ellipticity of the fiber can be calculated during the fiber fabrication. Second measurement is done by a tension meter to see the stress level in the fiber and the preform experiencing during the drawing process. Keeping stress at certain levels allows a consistent fiber drawing. Hence, these real-time measurement systems

Figure 3.30: PBG fibers are drawn in this fiber tower which is custom built by Bayindir Research Group.

are crucial components of the whole drawing system.

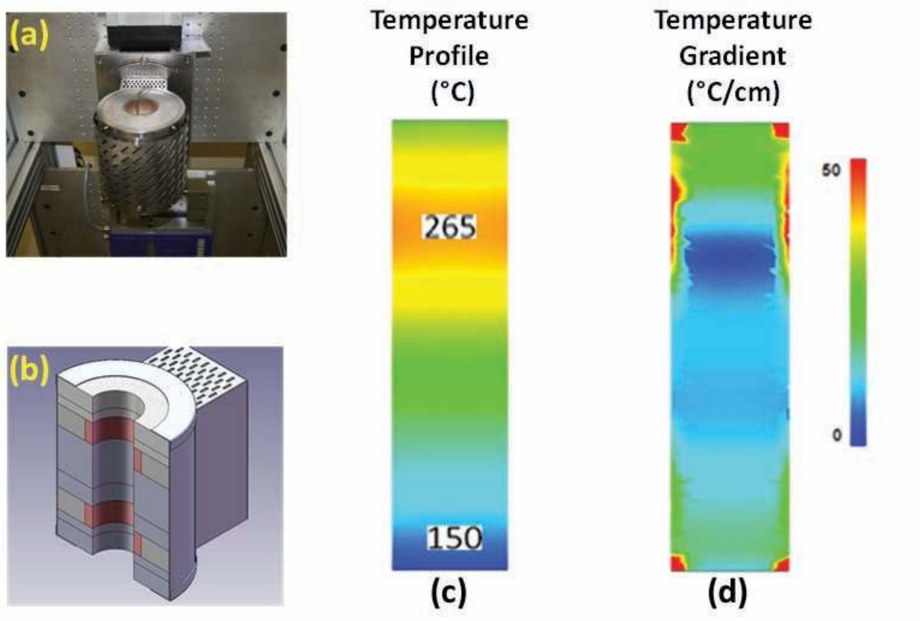

Figure 3.31: (a) A general picture of two zone oven used for heating preform. (b) Schematics of cross section of the oven. The red areas represent heating parts of the oven. (c) Temperature profile of inside of the oven when top zone is set to 290 °C and bottom zone is set to 200 °C. (d) Temperature gradient on the vertical cross sectional area of the oven.

The heating system of the fiber tower consists of two zone cylindrical heating oven (Fig. 3.31a and b). The top zone is adjusted to a temperature at which the the material gets soften and the bottom zone is adjusted in order to have a slowly changing ambient temperature. For As_2Se_3/PES material set the top zone is adjusted to 290-295 °C and the bottom zone is adjusted to 200 °C. Heating simulations of the oven is done using a Femlab Comsol software package. Simulations showed that if the set values for the zones are 290 °C and 200 °C, the actual temperatures at the center would be about 265 °C and 150 °C (Fig. 3.31). Temperature gradient also has big importance since, a proper fiber drawing is done under a very slowly changing temperature profile. Oven has an inner diameter of 5 cm and an outer diameter of 15 cm with a height of 18 cm. The top zone starts after 2 cm from the top and has a height of 4 cm. Similarly, the bottom zone starts after 2 cm from the bottom and has a height of 4 cm. The drawing is done at the 6 cm length in between the heating zone and presumably closer to the top zone. According to Fig. 3.31 temperature gradient is close to zero at this range. Hence, the design of the oven seems right for our purpose. In order to draw a fiber from a preform, preform should be placed axially aligned with the oven. Heating of the preform is done in steps because sudden temperature changes can result in uncontrolled deformations in the preform. For this reason, both zones are heated to 200 °C with 15 °C/min. Subsequently, temperature of the top zone is increased to drawing temperatures for 2 °C/min increase rate. The actual temperature can deviate depending on the precise size of the preform, ambient temperature and air circulation. Hence, the precise temperature setting is done during the drawing process. Experiments have shown that optimum drawing temperature is around 290 ±3 °C. During the heating process a constant stress of 200 g is applied to the bottom end of the preform until PES polymer starts to soften. After the softening begins preform feeding is started.

The drawing parameters are adjusted using kinematics and dynamics of the drawing procedure. The beginning point is conservation of materials during drawing. The total amount of material that is fed in the preform, should be equal to total amount of material that is in the fiber form. Eq. 3.12 is derived from material conservation. R_o and R_i represent outer and inner radii of preform and r_o and r_i represent outer and inner radii of fiber; V and ν are preform feeding and fiber drawing speeds, respectively (Fig. 3.32). The ratio of preform outer diameter to fiber outer diameter is called as reduction factor. However, inner radius is not reduced with the same rate and there is a collapse factor defined in Eq. 3.13. Using these relations, a proportionality factor can be derived (Eq. 3.14) which gives the length of fiber (l) using length of preform (L); $l = \frac{1}{\gamma}L$. These equation are derived using kinematic relations of the drawing process.

$$\nu = \frac{R_o^2 - R_i^2}{r_o^2 - r_i^2} V \tag{3.12}$$

$$r_o = RR_o, \qquad r_i = CRR_i \tag{3.13}$$

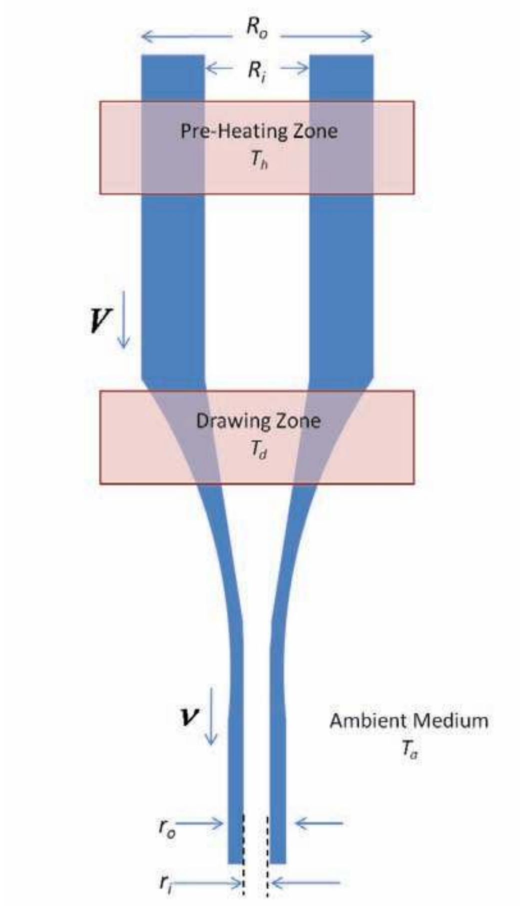

Figure 3.32: Schematic representation of drawing parameters.

$$\nu = \gamma V, \quad \texttt{where } \gamma = \frac{1}{R^2}\frac{1-\alpha}{1-\alpha C^2} \texttt{ and } \alpha = \frac{R_o^2}{R_i^2} \tag{3.14}$$

During the drawing process a stress is applied to the fiber. Multiplication of this stress with the fiber area gives the tension on the fiber; $T = \sigma A$ where A is the cross sectional area of the fiber. The strain rate is found as $\frac{d\epsilon}{dt} = \frac{\nu - V}{V}$. Together with the Trouton relation (Eq. 3.6) dynamic equation of the drawing process is found as in Eq. 3.16.

$$A = R^2\left(R_o^2 - C^2R_i^2\right) \tag{3.15}$$

$$T = 3\eta\frac{\nu - V}{V}R^2\left(R_o^2 - C^2R_i^2\right) \tag{3.16}$$

Kinematic and dynamic equations of thermal drawing is given. Using these relation and QWS equation, the central wavelength of the optical band gap is given as; $\lambda = 4RCn_{PES}d_{PES}$ where d_{PES} is thickness of the polymer film which is coated with As_2Se_3. As mentioned above, the tension, temperatures and feeding and drawing speeds are monitored during drawing. Hence, a complete control of fiber production is provided and PBG fibers for high power CO_2 laser beam delivery are fabricated.

3.5.1 Characterization of PBG Fibers

Whole fiber fabrication process from theoretical calculations to thermal drawing is explained in the preceding sections. Although the overall process is very complex application of a step by step approach enabled a well consistent fiber production. However, fiber characterization is needed both during and after the drawing process. During thermal drawing, optical band of drawn fiber is determined using a Fourier Transform Infrared Spectrometer and drawing parameters are adjusted to shift optical band to 10.6 μm. After drawing, SEM images of cross sections of fibers are taken to ensure conservation of structural integrity and to measure layer thicknesses.

PBG fibers that are aimed to be produced in this study are mainly fabricated for high power laser delivery for medical applications. This means that fabricated fibers should have almost perfect structure and optical property for the safety of the medical procedures. Hence, a detailed characterization of fibers has crucial importance. For this reason, the first part of fiber characterization is done during thermal drawing. We aimed to have PBG fibers which operate exactly at 10.6 μm, i.e. optical band gap along radial direction is centered at 10.6 μm and spectral transmission band of fiber along its core is centered at 10.6 μm. If transmission band of fiber is bigger than 10.6 μm, diameter of the fiber should be reduced in order to reduce layer thicknesses and decrease center wavelength. Similarly, if transmission band is smaller, diameter of the fiber should be increased. Normalized transmission spectra of three different fibers drawn from the same preform are given in Fig. 3.33. The dip in the transmission at 9.8 μm is the result of absorptions in the polymer. In conclusion, using FTIR measurements of fiber during drawing process enables immediate adjustment of drawing parameters and having fibers with desired optical band without any material and preform loss.

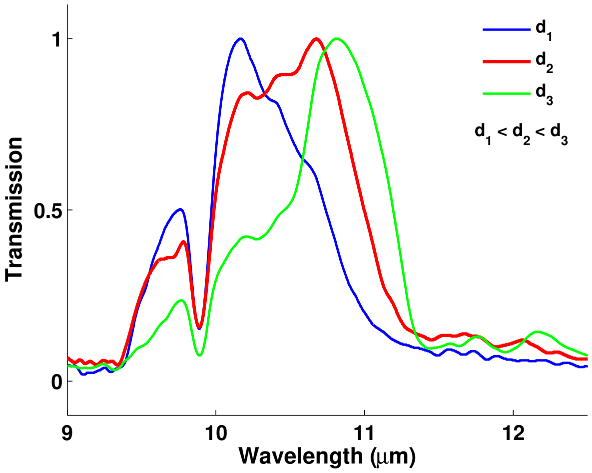

Figure 3.33: Transmission bands of three fibers drawn from the same preform.

Electron microscopy of fiber cross section is much complicated and long process. Sample preparation for scanning electron microscopy is done using a Leica EM FC6 model ultramicrotome (Fig. 3.34a) which is used for cutting of samples mechanically for precise sample preparation for microscopic characterization. Cutting of the sample can be done with different types of knifes such as diamond and glass knifes depending the material and the process. For our study, glass knifes are used for rough cutting and diamond knifes are used to have a very clean fiber cross section. Samples of fibers for scanning electron microscopy are prepared using ultramicrotome in order to have clean images of mirror layers and general structure of the fiber. For this purpose, small samples of fibers are embedded in a resin which is prepared by mixing Leica infiltration and Leica historesin hardener with a volumetric ratio of 15/1. This mix is put into a capsule together with the fiber and left for two hours for solidification of the resin (Fig. 3.34b). Then, samples are placed into the microtome and fibers are cooled to −120 °C. Here, before cooling core of the fibers are filled with alcohol/water mixture in order to prevent collapse of dielectric layer during the cutting process. At −120 °C we had a complete solid structure for ultra-thin cutting process. First, glass knifes are used for flattening the cross section and diamond knifes are used to have a perfectly clean and smooth surface.

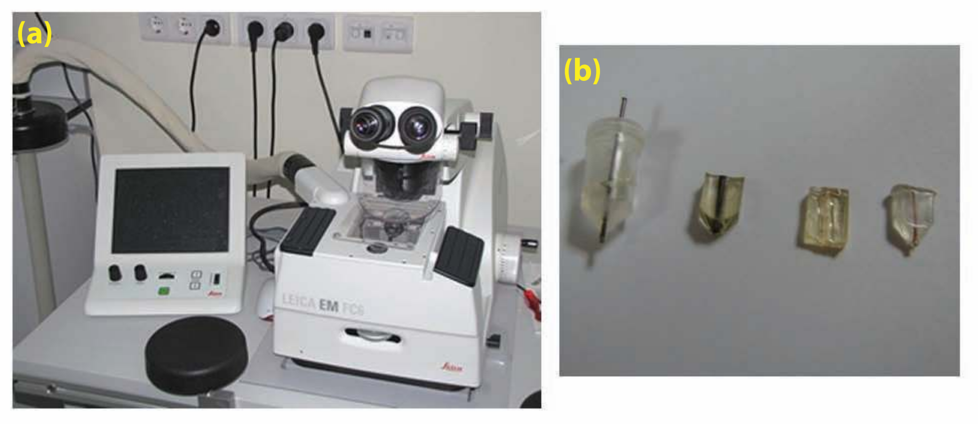

Figure 3.34: (a) The Leica EM FC6 Ultramicrotome used for sample preparation for electron microscopy. (b) Different fiber structure embedded into epoxy resin.

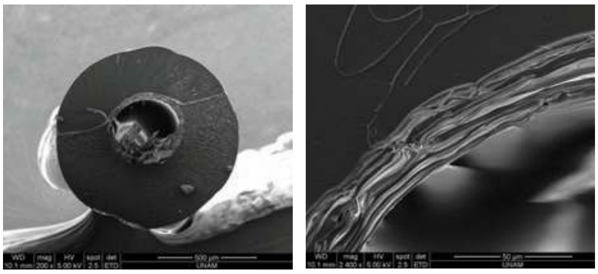

Figure 3.35: SEM images of a fiber cross section which is not prepared with microtome. (Drawing date: November, 2008)

The best method for cross sectional characterization of fibers is scanning electron microscopy. Samples with clean cross sections are placed in a FEI Quanta 200 FEG SEM system (Fig. 3.37). This system enables three different vacuum modes for specific kinds of samples. For example, conductive samples are examined under high vacuum (10^{-5} Torr) whereas dielectric samples such as PBG fibers are examined under low vacuum (1 Torr) without any need for conductive coating on the sample. The third mode is the environmental mode (1-20 Torr) which is used for the samples which are much sensitive to electron beam.

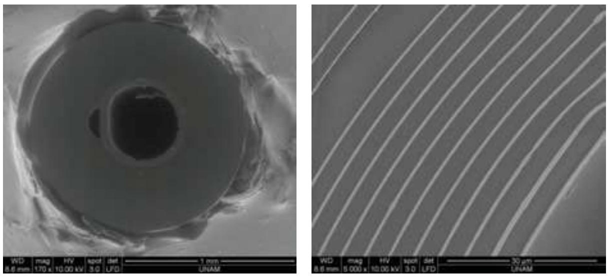

Figure 3.36: SEM images of a fiber cross section prepared with ultra-microtomy. (Drawing date: December, 2009)

SEM images of the samples and so ultramicrotomy is a crucial step of the whole study which gives a clear result of the micro structure on the inner surface of the fiber. Fig. 3.35 is an SEM image of a PBG fiber which is cut by hand and microtome is not used during sample preparation. As it can be seen from the figure, without high precision cutting all of the mirror structure is deformed and no conclusion can be done about micro structure of the dielectric mirror. Thus, through this study cryogenic ultramicrotomy is used for all drawn fibers. A better prepared sample is given in Fig. 3.36. In the figure it is seen that, the mirror structure is peeled off from the cladding structure. This indicates that the consolidation temperature during preform preparation is low. Hence, consolidation temperature is increased for about 2 °C to 257 °C. However, layers of the mirror structure are clean and uniform along all directions from axis of the fiber i.e. structural integrity during thermal drawing is conserved. Fig. 3.37 gives SEM images of fibers drawn with all-optimized production procedure.

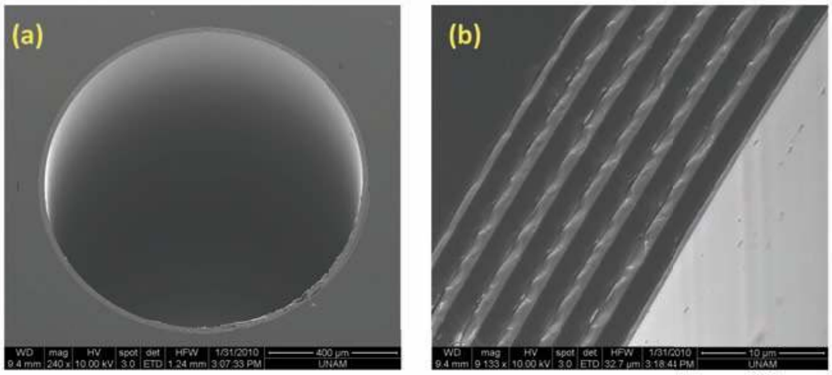

Figure 3.37: SEM images of a CO_2 fiber core (a) and layers of dielectric mirror (b).

Fig. 3.38 gives FTIR measurements and calculated transmissions of fibers drawn from three different preforms. After first trials, our studies have shown that the length of the film; hence number of layers in the mirror should be increased. Fibers in Fig. 3.38b and 3.38c are fabricated using longer coated films. As it can be seen from the figures, number of pairs in the mirror structure increased from 8 to 13 and structural integrity is better for the last two fibers. Although calculated and measured transmission of these fibers are not close enough, cut-back power measurements of these fibers are good enough for industrialization of the production procedure.

Chemical structure of fibers are done by analyzing X-rays coming from the surface of the structure. Signal capture is done by EDAX brand energy dispersive spectroscopy (EDS) detector integrated to the SEM system. An X-Ray spectrum profile of a PBG fiber is taken using this system (Fig. 3.39). In Fig. 3.39(a) arsenic (As) and selenium (Se) peaks coming from As_2Se_3 layers are clearly seen in addition to carbon (C), sulfur (S) and oxygen (O) peaks coming from PES

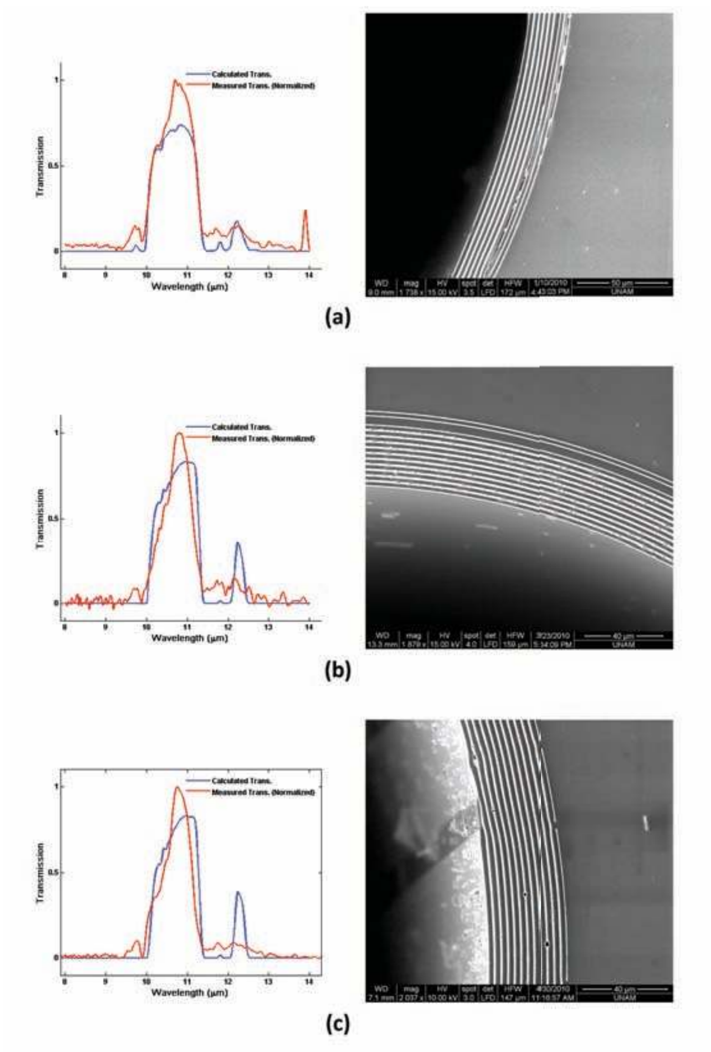

Figure 3.38: Normalized FTIR transmission measurements, calculated transmissions and SEM images of three different fibers drawn at different dates (a) 01.06.2010 b) 03.20.2010 c) 04.22.2010)

polymer. Furthermore, in Fig. 3.39(b) elemental mapping of cross section of same fiber is given. As it can be seen from the figure arsenic and selenium mapping of the structure is consistent with the SEM image of cross section of the fiber. Thus, during consolidation and drawing process, in addition to structural integrity, chemical structure of the materials are conserved.

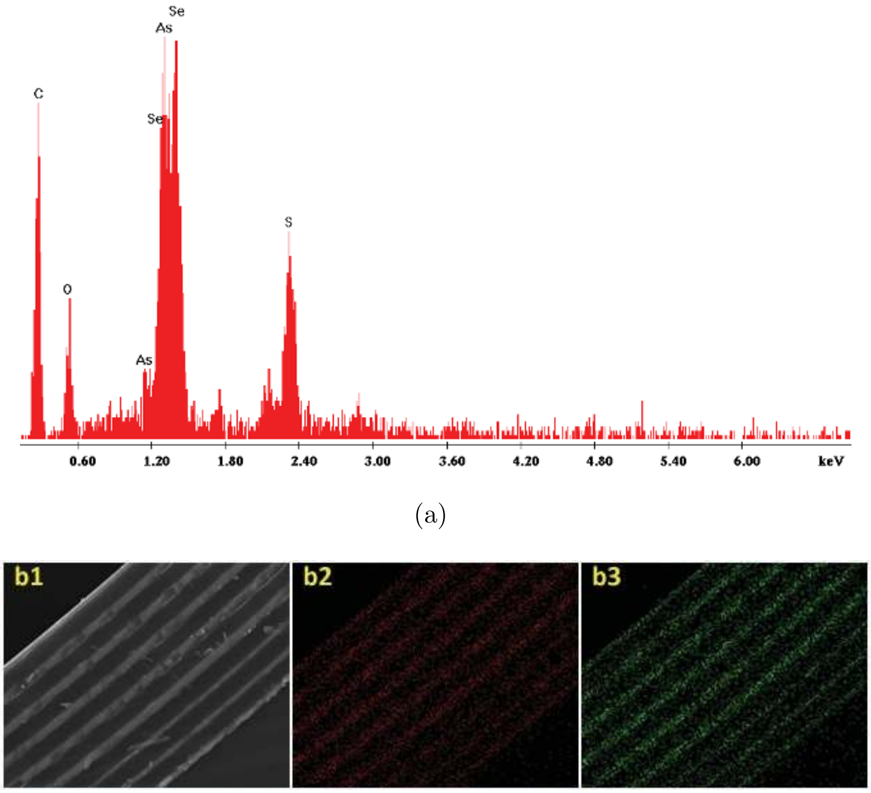

(a)

(b)

Figure 3.39: (a) X-Ray spectrum of a CO_2 laser fiber (Drawing date: 01.14.2010) (b) Chemical mapping of a CO_2 fiber (01.14.2010). (b1) SEM image; (b2) As mappping; (b3) Se mapping.

The drawing process is explained in detail in previous sections. During and after the drawing a well planned fiber characterization should be done for the final step of this study which is integration of newly designed PBG fibers to medical CO_2 laser systems. An FTIR measurement is done during the drawing process to ensure that transmission band of the fiber is around CO_2 laser frequency. Then, electron microscopy images of fiber cross sections are taken to see micro structure of photonic band gap structure; and finally chemical analysis of the fiber is done. Last step of fiber characterization and final purpose of this study is cut-back measurements of fibers integrated to CO_2 laser systems which is explained in the following chapter.

Chapter 4

Infrared Laser Beam Delivery

4.1 Current Status and System Review

The fabrication process and optimization steps of PBG fiber fabrication for high power laser delivery is explained in the previous chapters. From the materials to the end product i.e. PBG fiber, there are a lot of material concepts which are needed to be calculated in detail in order to deliver high power laser beam. After fabrication and characterization of the fiber, we needed to construct a system to couple CO_2 laser beam to waveguide structure which is provided by a multilayered dielectric film on the inner surface of the fiber. The laser system that is used in this study is a Lumenis C40 CO_2 laser system designed for medical applications (Fig. 4.1). Maximum power generated with Lumenis C40 is 40W which is enough for most majority of operations. This system originally guides laser beam to the tissue via lenses and mirrors inside a mechanical arm which enables the use of laser beam for open surgeries. The purpose of embedding a fiber guided laser system is to enable use of CO_2 laser beam for scarless surgeries with endoscopic applications.

The beam of Lumenis system has a diameter of 3 mm and the inner core of the fiber has a diameter of 0.8-0.9 mm depending on the production parameters. Thus the coupling can be provided by reducing the beam diameter. Before a

Figure 4.1: Lumenis C40 CO_2 laser system for medical application which is to be embedded with a laser beam coupling system.

complicated coupling of laser we first coupled the laser beam via a simple lens system (Fig. 4.2). For this reason we used a 0.5" diameter optical lens made of ZnSe with a focal length of 5". Wavelength range for the lens is 8-12 μm, hence it is a good choice for light beam focusing. We simply used the laser beam from Lumenis' mechanic arm and the lens for coupling. The main purpose for using this system is to see the effectiveness of fabrication process and the performance of the fiber. The problem here is the difficulty of using the system. For each time one need to adjust the lens and the beginning of the fiber core in very small scale using optical micrometer stages. As explained before, even though PES polymer has very small losses at 10.6 μm, high power of the laser beams burns polymer after certain time. Hence, focusing the laser light exactly into the core has significance importance. Another issue is radial surface of cut fiber. Experiments showed that fiber gets burned at the beginning point because scattering from the surface increases material absorption. Hence, smoothness of the surface should be provided. For this reason we used a water-alcohol solution and liquid nitrogen. We first filled the core of the fiber with the solution and expose it to very low temperatures. After the fiber gets brittle, with a sudden impact the fiber is cut. After this procedure, we annealed the fibers in vacuum oven at room temperature to get rid of any contamination caused by the solution.

Hence, the collapse of the mirror structure on the inner surface of the fiber is eliminated.

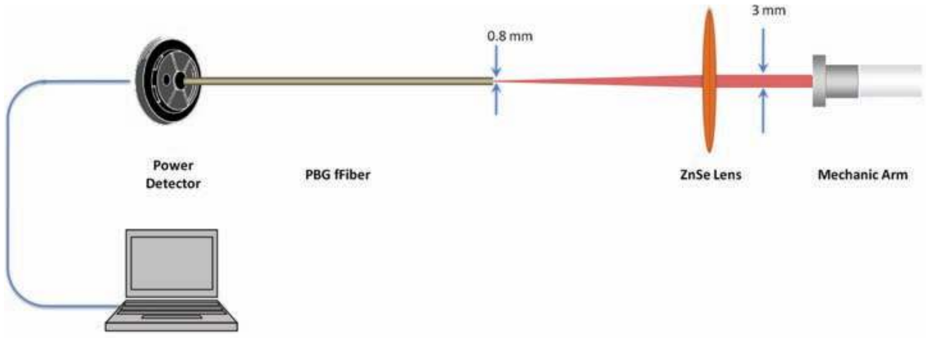

Figure 4.2: The basic laser coupling system used in this study before a complicated coupling system.

In order to provide accurate alignment of laser beam, a He-Ne laser beam (633 nm), coming from Lumenis and axially aligned with CO_2 laser beam, is used. The length of fibers are chosen to be around 1 m and to eliminate bending losses fibers are fixed in a straight position. At the end of fibers a Coherent FieldMaxII laser power meter is placed and transmitted laser power is measured with decreasing fiber lengths (cut-back measurements). Power is measured each time a 10 cm piece is cut from the fiber. Fig. 4.3 gives cut-back measurements of PBG fibers with simple coupling system. The losses are calculated using Eq. 4.1, where L is length of the fiber and I_{in} and I_{out} are incident and transmitted laser powers. Losses are found as -3.3 dB/m and -4.2 dB/m. Using this configuration we were able to transmit 15W laser beam. Losses in power transmission is resulted from materials absorption, especially absorptions in PES polymer, and alignment errors of optical axes of the lens, laser beam and axis of the fiber.

$$loss(\mathtt{dB}) = \frac{1}{L} 10\mathtt{log}_{10}\left(\frac{I_{out}}{I_{in}}\right) \tag{4.1}$$

The system given in Fig. 4.2 seems simple but it is not a good and quick way to couple laser beam to the fiber. We wanted to produce a system by which the fiber is mounted to the system with a quick and simple method with high efficiency beam coupling. In the next section the design of our coupling system will be explained.

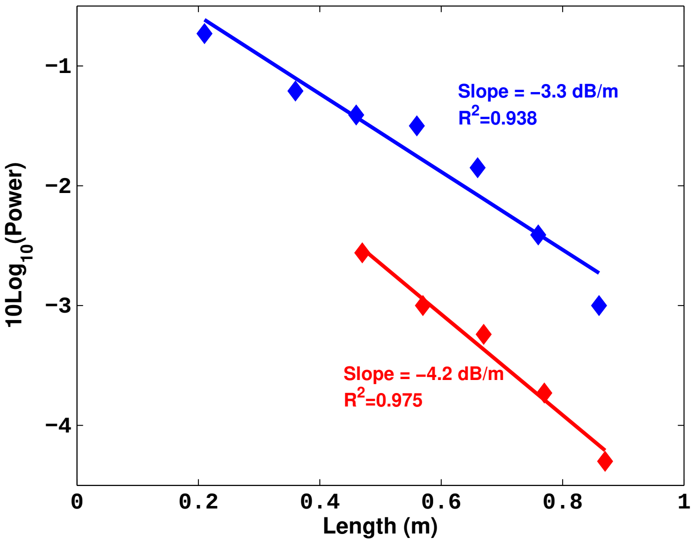

Figure 4.3: Power transmission data of a PBG fiber depending on the length of the fiber. Slopes of the lines give losses of the fibers.

4.2 New Coupling System

One of the purposes of this thesis is to propose an optimized laser application process for medical surgeries. Hence, the ease of use of the system becomes important. After fiber fabrication, the main problem is to couple laser light into the PBG fiber core through which light guiding is occurred. In order to produce an easy and efficient coupling a new design of fiber/laser system was necessary which should overcome with the following difficulties. First, alignment of the laser beam was vertical to the ground; so, a mirror should have been used to change the direction of the beam together with a micrometer displacement mechanism to change the tilt angles of the mirror. Second, the placement of the lens used for the reducing beam diameter. In order to have a radially symmetric beam, the lens should be placed on the optical axis exactly and distance between the lens and beginning of the fiber should be adjusted consistent with the focal length of the lens. Then, a fiber fixing mechanism should be used in order to place beginning of the fiber to the focus of the lens and fix the fiber at this point. Additionally, a fiber cooling should be done to keep temperature inside the core at low level to protect fiber's material integrity. A temperature rise in the core of the fiber can result in a physical deformation in the structure of fiber which can result in an optical performance failure. The last problem is material selection which should be done considering the ease of fabrication, costs and strength of the coupling system.

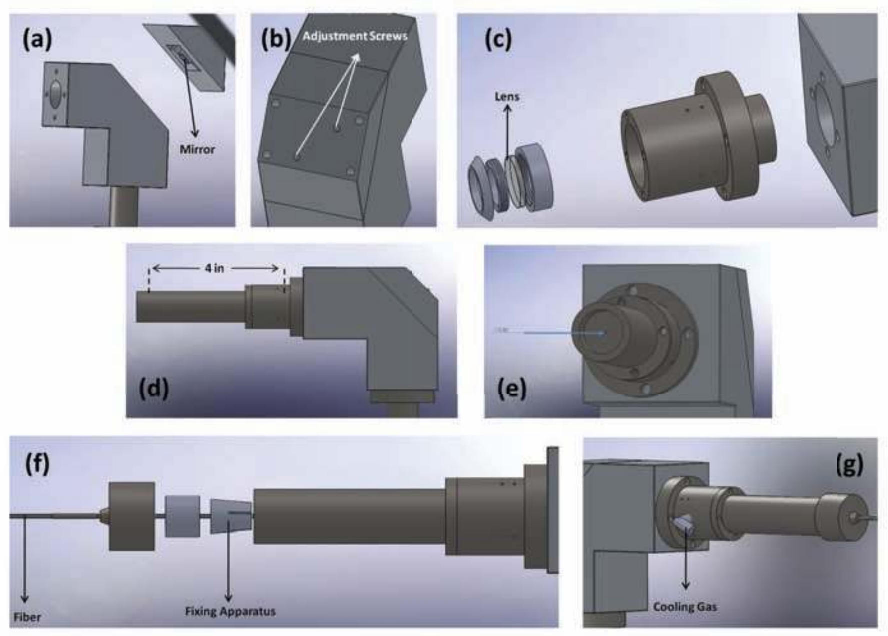

Figure 4.4: Design of the coupling system is done in steps each of which solve a particular problem. a) Direction change in the beam is done by a 45° tilted mirror. b) Adjustment screws are placed behind the mirror. c) A cavity is structure is designed in order to fix the lens which is transparent in the mid-IR region. d) Focal length of the lens is 4"; hence, distance between the fiber and the center of the lens determined accordingly. e) A 0.8 mm window is placed at the focal point of the coupling adapter to ensure the cladding of the fiber is not exposed to high power laser. f) A fiber fixing apparatus is designed to place fiber at the focal point of the lens and provide axial alignment. g) A simple gas valve is added to the system for gas cooling.

The steps of the designing process is determined by the particular problems that should be overcome. These steps are given in Fig. 4.4. The mirror is placed with an angle of 45° from the vertical to change the direction of the laser beam, and the adjustment of the mirror is done by a pair of screws placed behind the mirror. After that, a ZnSe lens is placed on the same axis with the beam. The diameter of the lens is 0.5" and the focal length is 4". This makes the distance between the lens and the fiber is also 4”. At the focal point of the lens a 0.8 mm window is placed. The purpose is to filter the laser light that falls on the cladding of the fiber and hence eliminate absorptions in the polymer. Beginning of the fiber is fixed in such a way that the core of the fiber and the window is aligned axially. As stated above, the last problem that should be solved is the cooling of the fiber core. For this reason the promising way is to use an inert gas to cool inside the fiber and experiments showed that He gas is the best choice; thus, a small gas valve is placed between the lens and the fiber. The last thing is the materials. In order to keep the device light and strong mechanical support parts are chosen to be Aluminum and the part where coupling occurs chosen to be steel. Fig. 4.5 is final form of the coupling system used for the laser transmission measurements.

Figure 4.5: An image of custom designed fiber coupler.

For loss measurements about 1m long fibers are chosen and ends of fibers are cut using an alcohol-water solution as explained above. After annealing prepared fibers in a vacuum oven, they are fixed into the adapter. During measurement fibers are fixed in a straight position to decrease bending losses and laser power at the other end of the fiber is measured using a Ophir Vega Digital Power-meter. Measurements are done at continuous wave mode. Additionally, a Flir Systems Thermovision A40 infrared camera is used to track heat profile of fibers through its length. Helium gas is used for cooling during the whole measurement process.

Using our custom designed coupling system, we were able to transmit 32 W with incident beam power of 40 W. Loss for this case is found as -0.6 dB/m which is a very good result for medical applications. Fig. 4.6 gives pictures of heat profile of fiber during laser transmission and burn of a wooden piece by laser output from the fiber.

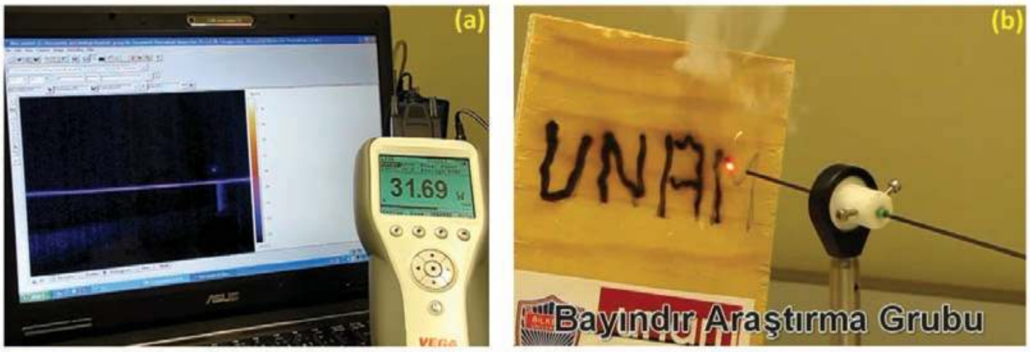

Figure 4.6: Heat profile of fiber during transmission of 40 W laser beam(with 32 W output power) (a) and burning of a wooden piece by output laser beam (b).

Table 4.1: Cut-back measurements data of PBG fiber using optimized fiber production and coupling system (Drawing date: 04.22.2010)

Length (m)	Power (W)			Average Power (W)
1.07	-	8.03	8.35	8.19
0.97	8.72	8.68	7.74	8.38
0.87	8.49	8.55	8.40	8.48
0.77	8.52	8.70	8.71	8.64
0.67	8.87	8.83	8.68	8.79
0.57	9.02	8.95	8.95	8.97
0.47	9.58	-	-	9.58

Table 4.1 is cut-back measurements data of 32 W fiber and Fig. 4.7 is the plot of the data. As it can be seen, loss of fibers are below 1 dB/m which is a satisfactory loss level for use of PBG fiber in medical operations. After system optimization and fiber characterization further study should be done on beam profile both ends of the fiber. Beam profiler is basically measures light intensity on a plane perpendicular to the propagation direction. Bram profiler used in this study is a Spiricon Pyrocam III beam profiler which scans a photo detector array on which laser light is coming. This beam profiler is very sensitive to high power beams; hence, we limited our laser power to 1 W. Beam profiles are taken before

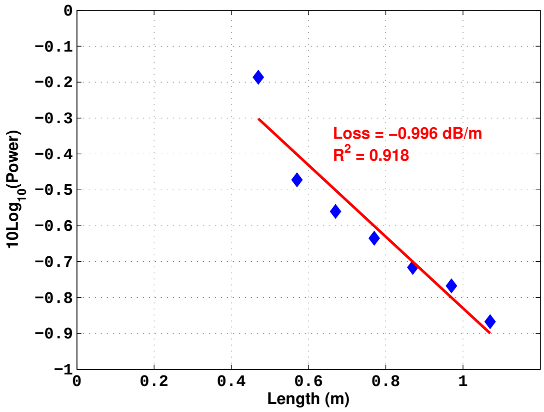

Figure 4.7: Cut-back measurements of highly efficient PBG fiber. Loss is found as -0.996 dB/m (Drawing date: 04.22.2010).

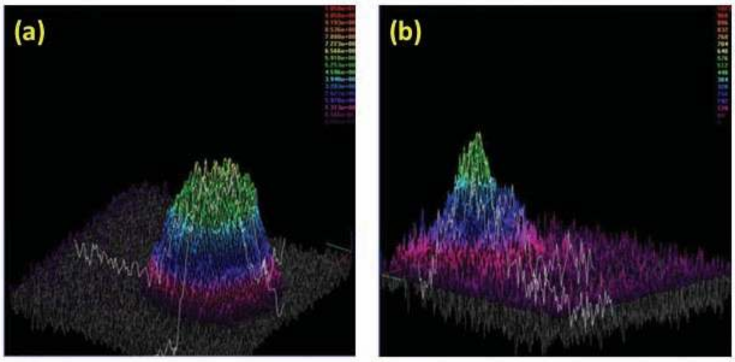

Figure 4.8: Profile of the beam after the lens in the coupler (a) and after transmitted through 1 m long PBG fiber (b) (Drawing date: 04.22.2010).

mounting fiber to the coupler and at the end of the fiber (Fig. 4.8). After the lens in the coupler profile of the beam has a Gaussian distribution whereas at the end of 1m long PBG fiber profile of the beam is distorted from Gaussian. Possible reasons arise from errors in axial alignment of fiber with the coupler, heating of the fiber during laser transmission and absorption of laser light in coupling adapter.

4.3 Measurements on Various Tissues

When temperatures in tissue reach above 100 °C, water in the cells start to boil and volume of the cells expand one-thousand-fold. Thus, the tissue breaks away explosively [66, 67]. In the tissue, laser-tissue interactions are depend on frequency of the laser beam, pulse durations, and power of the laser beam. In the case of CO_2 laser, laser beam is absorbed by a very thin layer of tissue (a few layers of cells) and the debris of the tissue forced out by the steam [9, 68]. Another important parameter for laser operations is optical constants of the tissue as well as transmission properties of the fiber used for laser beam transmission.

Due to beam, fiber and tissue properties, effects of lasers on tissue can be classified in different categories. First of these effects is *photothermal effect* which basically heat rise in tissue due to absorption of laser beam by the tissue. Heat rise can result in thermal denaturation of proteins at temperatures higher than 42.5 °C, coagulation at 60 °C, disruption of collagen tissues, tissue whitening and shrinkage. *Photoablation effect* on the other hand is volatilization of tissue by laser beam like a cut of scalpel. It is defined as explosive vaporization of intracellular water. Here, tissue water acts as a heat-sink, limiting the temperature to 100 °C. Pulsed laser beams can create shock waves and distort tissue integrity. Such effects are called *photoacustic effects. Coagulation* and *evaporation* are other effects of laser beams on tissue [10, 11].

Infrared laser light especially 2 μm and higher wavelengths are highly absorbed by the water in the tissue. Thus, laser tissue interactions are basically interaction of laser beam with the water in the tissue. For this reason, penetration depth of IR laser beams are very small and only the tissue on the surface is affected by the laser beam [8]. Therefore, such lasers have mostly photoablation, coagulation and evaporation effects on the operating tissue.

Use of CO_2 laser for endoscopic surfaces are a big challenge and fibers are best way to transport laser light to such organs. Fibers are used for laser transmission to larynx, pharynx, esophagus, bronchi, stomach, pancreas, urethra, prostate, uterus, etc. Thus, highly efficient CO_2 laser beam transmission is very important for a lot of endoscopic operations. In this case, proposal of laser transmission by hollow-core PBG fibers is a milestone for fast operations and very short healing times. In this study, we examined the current status of PBG fibers in medicine and proposed an well designed PBG fiber and fabrication method [69, 26].

4.3.1 CO_2 Laser - Tissue Interactions

During CO_2 laser use in operations incidence angle, direction, power and operation mode of the laser beam should be adjusted according to optical properties of the tissue and purpose of the operation [10]. For soft tissue, there are mainly three regions after application of laser on tissue (Fig. 4.9). The outermost layer is charred layer where all the tissue is burned. Here the temperatures can reach 100-500 °C. Thickness of this layer is inversely proportional with laser radiation and is called necrosis. Vacuolated zone is created by explosion of water bubbles which have water vapor inside them. After evaporation of tissue water, shrinkage in the tissue is observed. Thickness of this region is mostly depend on absorption characteristics of the tissue. The innermost layer is the coagulation layer which takes a black color at 100 °C. During coagulation collagen gets denaturalized, blood vessels gets narrow and tissue gets gray-brown colors. Formation of this layer prevents blooding during the operation and accelerates healing process.

In biomedical studies FTIR spectroscopy provides easy, fast and harmless materials characterization. Characteristic IR bands of large biomolecules gives information about bond structure and optical properties of these biomolecules

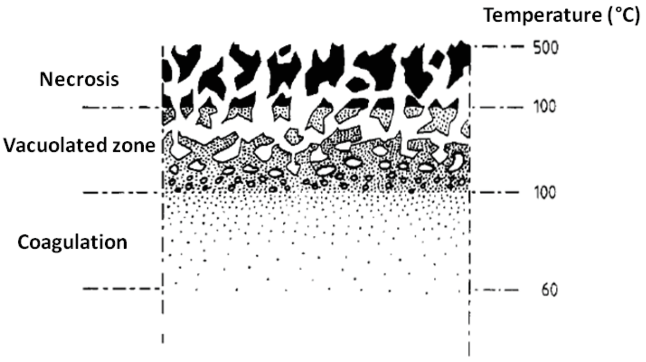

Figure 4.9: Laser ablation center and zones of laser tissue interaction.

[70]. Thence, structure and optical properties of organic molecules such as lipids, nucleic acids and carbohydrates can be obtained; and effect of laser on both healthy tissue and tumors can be examined in detail [71].

For applicability of CO_2 laser in medical operations, CO_2 laser beam is applied on same tissue parts and FTIR spectroscopy is taken from different regions in the vicinity of laser applied point.[1] 2W pulsed laser is applied with a pulse duration 0.1 seconds and FTIR data of the tissue at the applied point and 500 μm near the center (Fig. 4.10). It is found that spectroscopy of laser applied tissue and untouched tissue has similar characteristics. Peaks in both data are at the same frequency meaning that proteins in the tissue did not denaturate. The different between both data arises from small deviations of tissue thickness. This indicates that CO_2 laser beam does not damage near tissue.

Integration of PBG fibers to medical laser systems for easy light transmission is an important development in surgery, especially for endoscopic applications. Hence, ablation of unhealthy tissue can be done without big scars, damaging neighboring tissues and results in bloodless and painless small operations. Additionally using a gas coolant pumped through the fiber core enables transmission of laser light to very difficult places and removal of very small tumors. Use of lasers on retina and skin is very simple. However, laser operations on endoscopic tissue can only be possible with use of fibers; i.e. fibers are necessary for highly

---

[1] Laser-tissue interaction measurements were carried out by Ekin O. Ozgur by using flexible PBG fibers.

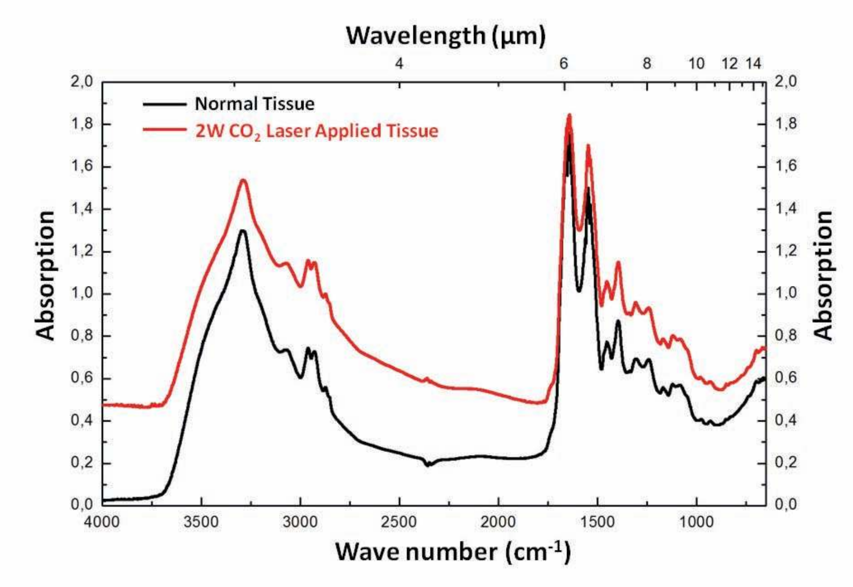

Figure 4.10: Comparison of normal muscle tissue and 2 W, 0.1 s pulsed laser applied tissue. There is not any significant structural change in the tissue.

efficient laser transmission to ears, nose, larynx, pharynx, esophagus, bronchi, stomach, pancreas, urethra, prostate, uterus, etc. Besides, with the improvements in minimally invasive surgery (Laparoscopic surgery), laser beams can be transported to brain, heart, arteries and even intestines [72].

First generation of fiber are used for transmission of UV, visible and near infrared laser light in continuous wave mode. Although there are many well developed fibers for such lasers, far infrared laser light is found to be best choice for endoscopic applications. In this study the purpose of design and fabrication of PBG fibers are to serve this purpose. Ho (2.1 μm) and CO_2 lasers are well known medical lasers operating at near and mid-infrared. This study is particularly focus on PBG fiber for CO_2 laser transmission.

4.3.1.1 Effect of CO_2 Laser on Cancerous and Healthy Lung Tissue

Most promising area for use of CO_2 laser fibers is lung tumor operations since bronchoscopy is already possible. Treatment of lung cancer is a very long and painful process and in the case of ablation of tumors, big body scars should be cut in order to reach unhealthy tissue. Development of a new and operation methods will decrease pain of the treatment and increase life standards of patients. In bronchoscopy, a metal tube is placed inside trachea and medical imaging can be conducted through this metal tube. Thus, a similar way can be used for ablation of tumors from trachea and large bronchi. As stated above, CO_2 laser has a coagulation effect in addition to tissue removal. Hence, choice of this laser for medical applications on lung tissue can decrease possibility of further complications after operations.

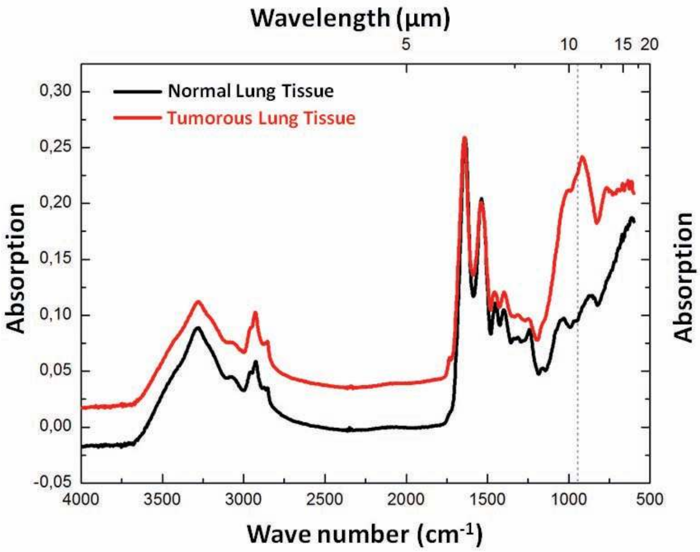

Figure 4.11: FTIR spectra of healthy lung tissue and lung tumor. At CO_2 laser wavelength (10.6 μm), absorption of tumor is significantly higher than normal tissue.

A detailed study on laser-tissue interactions is an important step for determination of certain parameters of laser operation. For this purpose, samples from tumorous human lung tissue are obtained and put into phosphate buffered saline (PBS) solution. Then, CO_2 laser is applied on these sample for different laser beam powers. FTIR data of laser applied tissues are taken using a Bruker Hyperion FTIR system. Results show that absorption constant of tumorous tissue is higher than from healthy tissue at 10.6 μm; i.e. effect of CO_2 laser on tumors are more damaging and control of operation can be done more easily (Fig. 4.11). In Fig. 4.12 images of CO_2 laser application using PBG fibers is given.

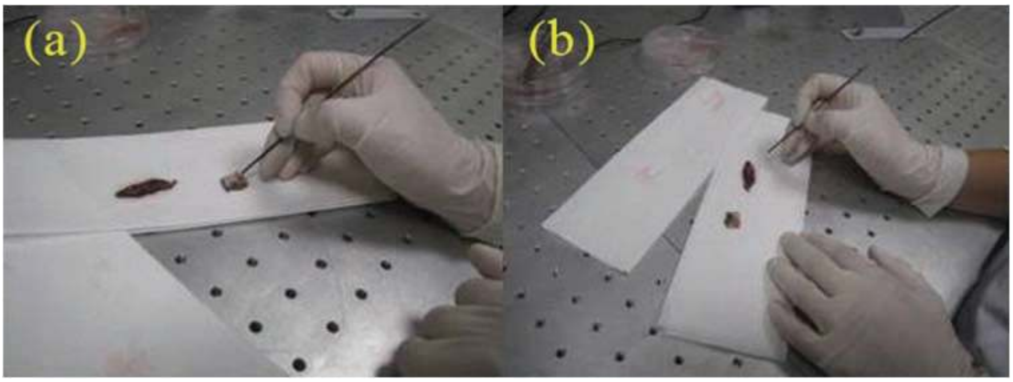

Figure 4.12: Laser application on tumorous (a) and healthy (b) lung tissue. Trials are done at different laser powers and different coolant He gas pressures.

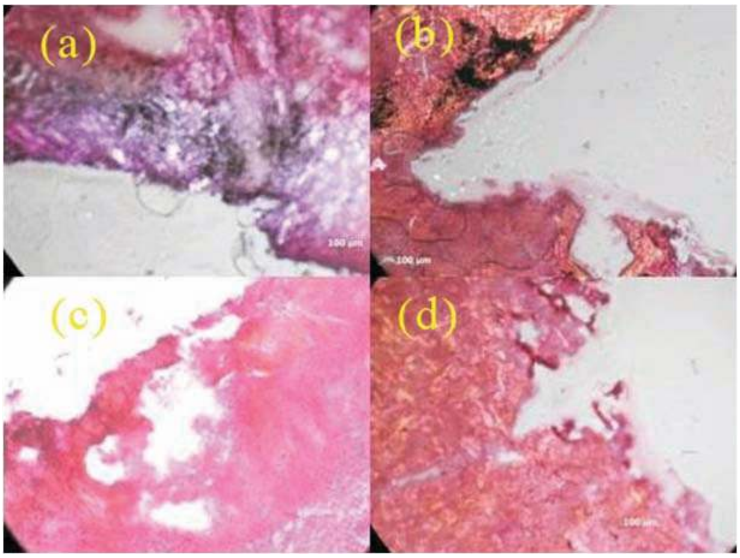

Figure 4.13: 1 W-cw laser beam applied tumor tissue (a), 2 W-cw laser beam applied tumor tissue (b), 1 W-cw laser beam applied healthy tissue (c), 2 W-cw laser beam applied healthy tissue (d). All laser applications are done with He gas coolant.

Laser applied tissues are then frozen at -25 °C and thin layers of samples are cut to see effect of laser beam. These thin samples are then dyed with hematoxylin and eosin stain (H&E stain) and optical images are taken using LEICA Axio Observer confocal microscope (Fig. 4.13). As it can be seen from the images, due to difference in absorptions of tumor and healthy tissue, tumors are burnt after application of 1 W and 2 W CO_2 laser. In addition, carbonized region in 2 W applied tissue is bigger compared to 1 W applied tumor tissue. On the other hand, healthy tissue is not affected from laser beam very much and it preserved its bright color.

For further examination of laser effects on lung tissue, a 3 W continuous wave laser beam is transmitted through a CO_2 laser PBG fiber (Drawing date: 04.17.2010) and fell on both tumor and healthy tissue. Then, electron microscopy images of these tissue sample are captured in environmental SEM system. This 3W laser created carbonized regions on and changed structure of tissues. I is observed that due to photothermal effects structural integrity of the tissue is damaged and the tissue shrank upon laser application.

Chapter 5

Summary and Future Work

Throughout this thesis it is stated that PBG fiber structures are strong candidates for the replacement of conventional high power delivery optical fibers since PBG fibers can provide wider wavelength range from near infrared to far infrared. One of the reasons is most of the tissues include high amounts of water and it is possible to ablate, coagulate and shrank tissue by applying laser light to heat up water molecules.

The beginning of PBG fabrication is calculations of theoretical aspect of optical phenomena created by photonic structures on the inner surface of PBG fiber. For this purpose, we simple use consecutive summation of reflections from each interface in a multilayered dielectric film. Such summations can be written in matrix formalism which enabled optical band gap calculations. After theoretical calculations we moved on to material characterization and we examined thermomechanical and optical properties of candidate materials. Measurements of thermal constants, viscosity calculations and refractive index measurements indicated that best material set for high power laser delivery, particularly CO_2 laser is As_2Se_3 ans PES. Then further examination of these materials are done for large area thin film formation and preform preparation. In order to fabricate highly efficient PBG fibers a series of system improvements are done such as film uniformity improvement, tube choice and film length increase. These improvements and highly controlled fabrication steps enabled fiber production with loss levels

>1 dB/m. 32 W output power from PBG fibers are reported. Finally, to see the effectiveness of CO_2 laser on healthy and cancerous tissues, laser-tissue interactions are examined. It is observed that absorption of tumor cells around 10.6 μm wavelength is significantly higher than healthy tissue. That is the reason why CO_2 laser is often used in medical operations such as tumor ablation. Through this study we proposed that fabrication of low-loss PBG fibers which can transmit high laser power can enable endoscopic operations; and hence, decrease pain and healing time.

The dielectric mirror structure on the inner surface of PBG fibers has a simple structure whereas has very useful optical property. By using simple one dimensional structure one can have an optical band gap for all incidence angles. Embedding impurities to layer thicknesses can create optical filters for specific wavelengths [26]. The cylindrical geometry has also many applications such as gas sensing [6] and lasing action by using an active layer [73]. Besides optical band gap structure, embedding new materials with different characteristics can effect function of the fiber. For instance, GAST glass used in this study has a changing refractive index with changing temperature. Hence, having a cavity layer made of GAST can be used as a tuned optical filter with changing temperature [74].

In addition to filtering mechanisms, it is also possible to use the optical cavity created in the hollow core of the fiber. Coating inner surface of the fiber with an active layer can result in a lasing action [73]. An active layer can also be used for frequency conversion of light that falls on outer surface of the fiber; which can concentrate light intensity to the end points of the fiber. Thus, a solar concentrator in fiber geometry can be fabricated although such work needs very detailed materials analysis and many trials. For example, choice of active layer, integrating such material into fiber geometry and engineering optical band gap according to the active layer are the most evident challenges of this device.

In the Introduction chapter we explained the objective of this thesis as high power laser delivery with very low loss levels. Fiber characterizations and power measurements showed that theoretical calculations, fiber design and fabrication resulted in highly efficient PBG fibers for CO_2 laser beam delivery. Results suggests that the next step in this study will be clinical trials of such fibers. Additionally, physical aspects of PBG fibers opens a wide gate for many different application areas from lasing action to solar energy conversion.

Bibliography

[1] Y. Fink, Daniel J. R., S. Fan, C. Chen, J. D. Joannopoulos, and E. L. Thomas. Guiding optical light in air using an all-dielectric structure. *Journal of Lightwave Technology*, 17(11):2039–2041, 1999.

[2] J. A. Harrington. A review of ir transmitting, hollow waveguides. *Fiber Integrated Optics*, 19:211, 2000.

[3] J. A. Harrington and C. C. Gregory. Hollow sapphire fibers for the delivery of co2 laser energy. *OSA, Optics Letters*, 15(10):541–543, 1990.

[4] R. F. Cregan, B. J. Mangan, J. C. Knight, T. A. Birks, P. St. J. Russell, P. J. Roberts, and D. C. Allan. Single-mode photonic band gap guidance of light in air. *Science*, 285:1537–1539, 1999.

[5] Y. Fink, J. N. Winn, S. Fan, C. Chen, J. Michel, J. D. Joannopoulos, and E. L. Thomas. A dielectric omnidirectional reflector. *Science*, 282:1679–1682, 1998.

[6] A. Yildirim, M. Vural, M. Yaman, and M. Bayindir. Bioinspired optoelectronic nose with nanostructured wavelength-scalable hollow-core infrared fibers. *Advanced Materials*, 23(10):1262–1262, 2011.

[7] O. S., K. Kuriki, N. D. Orf, A. F. Abouraddy, G. Benoit, J. F. Viens, A. Rodriguez, M. Ibanescu, J. D. Joannopoulos, and Y. Fink. Surface-emitting fiber lasers. *OSA Optics Express*, 14(9):3923–3935, 2006.

[8] C. J. M. Moes, M. J. C. van Gemert, W. M. Star, J. P. A. Marijnissen, and S. A. Prahl. Measurements and calculations of the energy fluence rate in a

scattering and absorbing phantom at 633 nm. *Appl. Opt.*, 28(12):2292–2296, Jun 1989.

[9] G. Muller, W. Wasche, U. Bindig, and K. Liebold. Ir-spectroscopy for tissue differentiation in the medical field. *Laser Physics*, 9:348–356, 1999.

[10] Q. Peng, A. Juzeniene, J. Chen, L. O. Svaasand, T. Warloe, K.-E. Giercksky, and J. Moan. Lasers in medicine. *Rep. Prog. Phys.*, 71, 2008.

[11] A. L. McKenzie. A three-zone model of soft-tissue damage by a co_2 laser. *Physics in Medicine and Biology*, 31(9):967, 1986.

[12] B. Temelkuran, S. D. Hart, G. Benoit, J. D. Joannopoulos, and Y. Fink. Wavelength-scalable hollow optical fibres with large photonic bandgaps for co_2 laser transmission. *Nature*, 420:650–653, 2002.

[13] M. Bayindir, A. F. Abouraddy, J. Arnold, J. D. Joannopoulos, and Y. Fink. Thermal-sensing fiber devices by multimaterial codrawing. *Advanced Materials*, 18:845–849, 2006.

[14] A. F. Abouraddy, M. Bayindir, G. Benoit, S. D. Hart, K. Kuriki, N. Orf, O. Shapira, F. Sorin, B. Temelkuran, and Y. Fink. Towards multimaterial multifunctional fibres that see, hear, sense and communicate. *Nature Materials*, 6:336–347, 2007.

[15] M. Bayindir, O. S., D. Saygin-Hinczewski, J. Viens, A. F. Abouraddy, J. D. Joannopoulos, and Y. Fink. Integrated fibres for self-monitored optical transport. *Nature Materials*, 4(12):820–825, 2005.

[16] D.A. Alsberg, J.C. Bankert, and P.T. Hutchison. The wt4/wt4a millimeter wave transmission system. *Bell Syst. Tech. J.*, 56:1849, 1977.

[17] J. W. Strutt. On the maintenance of vibrations by forces of double frequency, and on the propagation of waves through a medium endowed with a periodic structure. *Philosophical Magazine*, 24(147):145–159, 1887.

[18] J. W. Strutt. On the reflection of light from a regularly stratified medium. *Proceedings of Royal Society*, 93:565–577, 1917.

[19] P. Yeh, A. Yariv, and C. S. Hong. Electromagnetic propagation in periodic stratified media. i. general theory. *JOSA*, 67(4):423–438, 1977.

[20] Pochi Yeh. *Optical Waves in Layered Media.* Wiley-Interscience Publications, USA, 1988.

[21] J. N. Winn, Y. Fink, S. Fan, and J. D. Joannopoulos. Omnidirectional reflection from a one-dimensional photonic crystal. *OSA Optics Letters*, 23(20):1573–1575, 1998.

[22] J. D. Joannopoulos, P. R. Villeneuve, and S. Fan. Photonic crystals: puttin a new twist on light. *Nature*, 386:143–149, 1997.

[23] B. E. A. Saleh and M. C. Teich. *Fundamentals of Photonics.* Wiley-Interscience Publications, USA, 1991.

[24] G. Benoit, K. Kuriki, J.-F. Viens, J. D. Joannopoulos, and Y. Fink. Dynamic all-optical tuning of transverse resonant cavity modes in photonic bandgap fibers. *OSA Optics Letters*, 30(13):1620–1622, 2005.

[25] G. Benoit, S. D. Hart, B. Temelkuran, J. D. Joannopoulos, and Y. Fink. Static and dynamic properties of optical microcavities in photonic bandgap yarns. *Advanced Materials*, 15(24):2053–2056, 2003.

[26] H. E. Kondakci, M. Yaman, O. Koylu, A. Dana, and M. Bayindir. All-chalcogenide glass omnidirectional photonic band gap variable infrared filters. *Applied Physics Letters*, 94:111110, 2009.

[27] M. Ibanescu, Y. Fink, S. Fan, E. L. Thomas, and J. D. Joannopoulos. An all-dielectric coaxial waveguide. *Science*, 289(5478):415–419, 2000.

[28] J. D. Joannopoulos, S. G. Johnson, J. N. Winn, and R. D. Meade. *Photonic Crystals: Molding the flow of light (Second ed.).* Princeton University Press, N.J., 2006.

[29] P. St. J. Russell. Photonic crystal fibers. *Science*, 299:358–362, 2003.

[30] J. Knight. Photonic crystal fibres. *Nature*, 424:847–851, 2003.

[31] R.D. Maurer and P.C. Schultz. Fused silica optical waveguide. United States Patent No. 3,659,915, February 1972.

[32] M. Miyagi, A. Hongo, Y. Aizawa, and S. Kawakami. Fabrication of germanium-coated nickel hollow waveguides for infrared transmission. *Applied Physics Letters*, 43:430, 1983.

[33] H. Taniyama. Waveguide structures using one-dimensional photonic crystal. *Journal of Applied Physics*, 91(6):3511–3515, 2002.

[34] M. Bayindir, B. Temelkuran, and E. Ozbay. Tight-binding description of the coupled defect modes in three-dimensional photonic crystals. *Physical Review Letters*, 84(10):2140–2143, 2000.

[35] P. Vukusic and J.R. Sambles. Photonic structures in biology. *Nature*, 424(6950):852–855, 2003.

[36] A. W. Snyder and J. D. Love. *Optical Waveguide Theory*. Chapman and Hall, N.Y., 1983.

[37] E. Yablonovitch, T. J. Gmitter, and K.M. Leung. Photonic band structure: The face-centered-cubic case employing non-spherical atoms. *Physical Review Letters*, 67(17):2295–2298, 1991.

[38] E. Lidorikis, M.L. Povinelli, S.G. Johnson, and J.D. Joannopoulos. Polarization-independent linear waveguides in 3d photonic crystals. *Physical Review Letters*, 91(2), 2003.

[39] A. Chutinan and S. Noda. Design for waveguides in three-dimensional photonic crystals. *Japanese Journal of Applied Physics*, 39:2353–2356, 2000.

[40] F. Desevedavy, G. Renversez, J. Troles, P. Houizot, L. Brilland, I. Vasilief, Q. Coulombier, N. Traynor, F. Smektala, and J.-L. Adam. Chalcogenide glass hollow core photonic crystal fibers. *Optical Materials*, 32(11):1532–1539, 2010.

[41] F. C. Holsinger, C. N. Prichard, G. Shapira, O. Weisberg, D. S. Torres, C. Anastassiou, E. Harel, Y. Fink, and R. S. Weber. Use of the photonic

band gap fiber assembly co_2 laser system in head and neck surgical oncology. *Laryngoscope*, 116(7), 2006.

[42] J.B. Macchesney and P.B. O'connor. Optical fiber fabrication and resulting product. United States Patent No. 4,217,027, August 1977.

[43] C. M. Smith, N. Venkataraman, M. T. Gallagher, D. Muller, J. A. West, N. F. Borrelli, D. C. Allan, and K. W. Koch. Low-loss hollow-core silica/air photonic bandgap fibre. *Nature*, 424(6949):657–659, 2003.

[44] S. D. Hart, G. R. Maskaly, B. Temelkuran, P. H. Prideaux, J. D. Joannopoulos, and Y. Fink. External reflection from omnidirectional dielectric mirror fibers. *Science*, 296:510–513, 2002.

[45] S. D. Hart. *Multilayer Composite Photonic Bandgap Fibers.* PhD thesis, Massachusetts Institute of Technology, 2004.

[46] L. Cognolato. Chemical vapour deposition for optical fibre technology. *J. Phys. IV France*, 5:975, 1995.

[47] A. Dhar, A. Pal, M. C. Paul, P. Ray, H. S. Maiti, and R. Sen. The mechanism of rare earth incorporation in solution doping process. *Opt. Express*, 16(17):12835–12846, Aug 2008.

[48] M. Leich, F. Just, A. Langner, M. Such, G. Schötz, T. Eschrich, and S. Grimm. Highly efficient yb-doped silica fibers prepared by powder sinter technology. *Opt. Lett.*, 36(9):1557–1559, May 2011.

[49] A. K. Varshneya. *Fundamentals of Inorganic Glasses.* Academic Press, N.Y., 1994.

[50] D. W. van Krevelen. *Properties of Polymers (4^{th} edition).* Elsevier Scientific, N.Y., 1990.

[51] D. W. van Krevelen. *Properties of Polymers, Their Estimation and Correlation with Chemical Structure (2^{nd} edition).* Elsevier Press, Amsterdam, 1976.

[52] J. C. Knight and P. S. Russett. Applied optics: New ways to guide light. *SCIENCE*, 296(5566):276–277, 2002.

[53] A. Bornstein and N. Croitoru. Experimental evaluation of a hollow glass-fiber. *Applied Optics*, 25:355, 1986.

[54] Z. U. Borisova. *Glassy Semiconductors*. Plenum Press, N.Y., 1981.

[55] F. T. Trouton. On the coefficient of viscous traction and its relation to that of viscosity. *Proc. Roy. Soc. London*, A 77:426–440, 1906.

[56] A. S. Tverjanovich. Temperature dependence of the viscosity of chalcogenide glass-forming melts. *Glass Physics and Chemistry*, 29:532, 2003.

[57] G. Yang, , T. Rouxel, J. Troles, B. Bureau, C. Boussard-Plèdel, P. Houizot, and J.-C. Sangleboeuf. Viscosity of As_2Se_3 glass during the fiber drawing process. *Journal of the American Ceramic Society*, pages no–no, 2011.

[58] Gordon S. Fulcher. Analysis of recent measurements of the viscosity of glasses. *Journal of the American Ceramic Society*, 8(6):339–355, 1925.

[59] P. J. Webber and J. A. Savage. Measurement of the viscosity of chalcogenide glasses by a parallel plate technique. *Journal of Materials Science*, 16:763–766, 1981.

[60] L. A. Cauchy. *Bull. des. sc. math*, 14:9, 1830.

[61] G. Andermann and L. R. Brantley. Cauchy analysis of imaginary-dielectric-index bands. *J. Opt. Soc. Am.*, 58(2):171–172, Feb 1968.

[62] R. Capan, N. B. Chaure, A. K. Hassan, and A. K. Ray. Optical dispersion in spun nanocrystalline titania thin films. *Semiconductor Science and Technology*, 19(2):198–202, Feb 2004.

[63] M. Vural. *Hollow core Photonic Band Gap Fibers For Medical Applicationn*. PhD thesis, Bilkent University, 2009.

[64] E. Lee. Simulation of the thin-film thickness distribution for an oled thermal evaporation process. *Vacuum*, 83(5):848 – 852, 2009.

[65] H. K. Pulker. *Coatings on Glass, 2nd ed.* Elsevier Science B. V., 1999.

[66] A. L. McKenzie. Physics of thermal processes in laser-tissue interaction. *Physics in Medicine and Biology*, 35(9):1175, 1990.

[67] T. Menovsky, J. F. Beek, and E. Chan. Laser-assisted nerve repair. *Plastic & Reconstructive Surgery*, 95:609, 1995.

[68] J. A. Dixon. Current laser applications in general surgery. *Annals of Surger*, 207:355–372, 1988.

[69] E. O. Ozgur, A. Yilmaz, and M. Bayindir. unpublished, 2010.

[70] S. Y. Lin, M. J. Li, and W. T. Cheng. FT-IR and raman vibrational microspectroscopies used for spectral biodiagnosis of human tissues. *Spectroscopy*, 21(1):1–30, 2007.

[71] P. N. R. Nair, M. Baltensperger, H. U. Luder, and G. K. H. Eyrich. Observations on pulpal response to carbon dioxide laser drilling of dentine in healthy human third molars. *Lasers in Medical Science*, 19(4):240–247, 2005.

[72] A. Ernst, D. Feller-Kopman, H. D. Becker, and A. C. Mehta. Central airway obstruction. *Am. J. Respir. Crit. Care Med.*, 169(12):1278–1297, 2004.

[73] O. Shapira, K. Kuriki, N. D. Orf, A. F. Abouraddy, G. Benoit, J. F. Viens, A. Rodriguez, M. Ibanescu, J. D. Joannopoulos, Y. Fink, and M. M. Brewster. Surface-emitting fiber lasers. *Opt. Express*, 14(9):3929–3935, May 2006.

[74] H. E. Kondakci, M. Yaman, A. Dana, and M. Bayindir. Photonic bandgap infrared spectrometer. *Appl. Opt.*, 49(18):3596–3600, Jun 2010.